THE ASTROPHYSICAL JOURNAL SUPPLEMENT SERIES, 129:61–92, 2000 July
© 2000. The American Astronomical Society. All rights reserved. Printed in U.S.A.

VERY LONG BASELINE POLARIMETRY OF BL LACERTAE

GRANT R. DENN AND ROBERT L. MUTEL
Department of Physics and Astronomy, University of Iowa, Iowa City, IA 52242; denn@gasou.edu, robert-mutel@uiowa.edu
AND
ALAN P. MARSCHER
Department of Astronomy, Boston University, Boston, MA 02215; marscher@bu.edu
Received 1999 May 14; accepted 2000 February 2

ABSTRACT

We present the results of an extensive observing campaign designed to study the evolution of parsec-scale radio structure in the nucleus of the AGN galaxy BL Lacertae. The observations spanned 17 epochs from 1994.7 to 1998.3. The VLBA observations, made at regular intervals at 15, 22, and 43 GHz, show the ejection and evolution of four highly polarized superluminal components (denoted S7–S10). The trajectories of all components were significantly curved, with the slowest component (S8) exhibiting the most bending. All four components had nearly constant apparent speeds, at least between 1 and 3 mas separation from the core. Extrapolation of the core-component separation to a zero spacing epoch suggests that they may have been created in pairs, with fast and slow counterparts. Each superluminal component was moderately linearly polarized at all observed frequencies. The electric vector position angle (EVPA) was frequency independent but changed with core-component separation for all four components, with total EVPA rotation varying from 30° (S7) to 80° (S8). There was no preferred EVPA orientation with respect to the jet axis when components were young, i.e., close to the core. However, three of the four components' EVPAs rotated to within 20° of the jet direction at later epochs, consistent with emission from transverse shocks. The core was nearly unpolarized at 15 GHz, except when a new superluminal component was just emerging. At higher frequencies (22 and 43 GHz) core fractional polarization was low with a quadratic frequency dependence. We applied Hardee's model of helical twisting on an adiabatically expanding jet to explain the observed bent component trajectories. By searching the parameter space of allowed helical geometries, we found a best-fit set of parameters with fixed opening and line of sight angles for all four components. The preferred helical geometry was described by a line of sight angle $\Theta \simeq 9°$ and a jet half-opening angle $\Psi \simeq 2°$. Individual component trajectories were fitted by varying initial conditions at the throat of the jet and the initial helical wavelength scale. Although the position along the jet and apparent speed are consistent with the helical model, the predicted polarization position angles are not in good agreement. We derived physical properties in the emission regions by assuming that they are due to optically thin synchrotron radiative shocks within a underlying relativistic flow. Using the observed fractional polarization and jet-interjet intensity ratio along with the helix-line of sight angle as constraints, we found that slower components (S8, S10) are consistent with forward shocks, while faster components (S7, S9) could be either forward or reverse shocks. Derived shock compression ratios vary from weak ($k \sim 0.5$–0.8) for slow component S8 to moderately strong ($k \sim 0.0$–0.5) for fast component S9. As of epoch 1998.2, there have been no unusual features in the parsec-scale radio structure following the large optical–gamma-ray flare at epoch 1997.6.

Subject headings: BL Lacertae objects: individual (BL Lacertae) — galaxies: jets — polarization — radio continuum: galaxies — techniques: interferometric

1. INTRODUCTION

Studies of the spatial distribution of polarized radio emission from the parsec-scale cores of active galactic nuclei (AGNs) can provide important information about the distribution and orientation of magnetic fields in these sources. Pioneering observations using full-polarization VLB arrays (VLBP) by Cotton et al. (1984) and the Brandeis group, e.g., (Roberts, Gabuzda, & Wardle 1987; Gabuzda, Wardle, & Roberts 1989; Gabuzda et al. 1992) showed that AGN cores themselves are often nearly unpolarized, while the jets, and especially the knots within the jets, are often significantly polarized. The magnetic field orientation in many knots is nearly perpendicular to the parent jet, suggesting that the knot component is a result of a transverse shock which has compressed the field normal to the shock propagation direction (Hughes et al. 1985). Some jet components have nearly parallel magnetic fields, suggesting that the fields have been stretched along the jet by shear forces.

Cawthorne et al. (1993) studied a sample of 12 quasars and eight BL Lac objects at 5 GHz from the Pearson-Readhead VLBI survey (Pearson & Readhead 1988) and concluded that there are systematic differences between quasars and BL Lac objects in the core polarization and orientation of the magnetic field in the jet. They found that the magnetic fields in the jets of quasars are predominantly parallel while those of BL Lac objects are perpendicular. This suggests that the although plane-perpendicular shocks may occur in both quasars and BL Lac objects, quasar shocks may be weaker so that the transverse field amplified by the shock does not dominate the mostly longitudinal polarization of the quasar jet. However, more recent VLBP studies of both BL Lac objects and quasars are not always consistent with this simple picture. Gabuzda & Cawthorne (1996) found a strongly polarized component in the BL Lac object 1219+285 with a magnetic field parallel to the jet, while Leppänen, Zensus, & Diamond (1995) found that the

inner components of the well-known quasars 3C 345 and 3C 279 have magnetic fields perpendicular to the jets. Using dual-frequency VLBP, Hutchinson & Cawthorne (1997) found that the 35° misalignment between the magnetic field and jet direction measured for the quasar 4C 71.07 by Cawthorne et al. (1993) could not be caused by Faraday rotation but was intrinsic.

In this paper we present the results of long-term VLBI monitoring program of the radio core of BL Lacertae. The observations started in late 1994 using global VLBI arrays using two frequencies and a single polarization. Starting in mid-1995, we utilized the more powerful VLBA array, allowing both simultaneous multifrequency and full polarization maps. We present maps and analysis of observations spanning a total of 20 epochs from 1994.73 to 1998.28. The maps show the ejection of several luminous, highly polarized superluminal components. In § 2, we describe our observations of BL Lac. In § 3, we present Stokes I, Stokes P, and fractional polarization maps of BL Lac, and we discuss the trajectories, apparent speeds, spectral characteristics, and polarization structure of the core and jet components. In § 4 we discuss a helical jet model for BL Lac and apply it to the observed trajectories, speeds, and polarization of superluminal knots. We also apply the relativistic shock model of Hughes et al. (1989) to estimate the shock strength and direction relative to the underlying jet flow. Finally, we discuss the optical and gamma-ray outburst during 1997 July and discuss the possible effect of this flare on parsec-scale radio jet observations.

Throughout this paper we adopt a value of $H_0 = 100\ h$ km s^{-1} Mpc^{-1} for the Hubble constant and $q_0 = 0.5$. Using BL Lac's measured redshift of $z = 0.069$ (Miller, French, & Hawley 1978) results in a luminosity distance $D_L = 210\ h^{-1}$ Mpc, and a corresponding image scale of 1 milliarcsecond (mas) = $0.89\ h^{-1}$ pc. The convention used for the frequency spectral index α is $S(\nu) \propto \nu^{\alpha}$.

2. OBSERVATIONS AND DATA REDUCTION

The compact radio structure of BL Lac was monitored using VLB arrays in two sets of observations from 1994 to 1998. The first monitoring program consisted of dual-frequency, single-polarization observations. The second monitoring program, starting in mid-1995, used the full VLBA at several frequencies and with full polarization. Table 1 summarizes the observation epochs and telescope arrays used for all observations.

2.1. *VLBA Observations (1994.78–1994.89)*

We observed BL Lac at 8.4 and 15.4 GHz on 1994 September 25 and November 3 using seven elements of the VLBA.[1] We included the 100 m telescope in Effelsberg at 8.4 GHz for the November session. The tapes were correlated at the JPL-Caltech Block II VLBI correlator and the data further reduced using the Caltech VLBI package. The editing, calibration, self-calibration, and hybrid mapping

[1] The VLBA is operated by the National Radio Astronomy Observatory which is managed by Associated Universities, Inc., under cooperative agreement with the National Science Foundation.

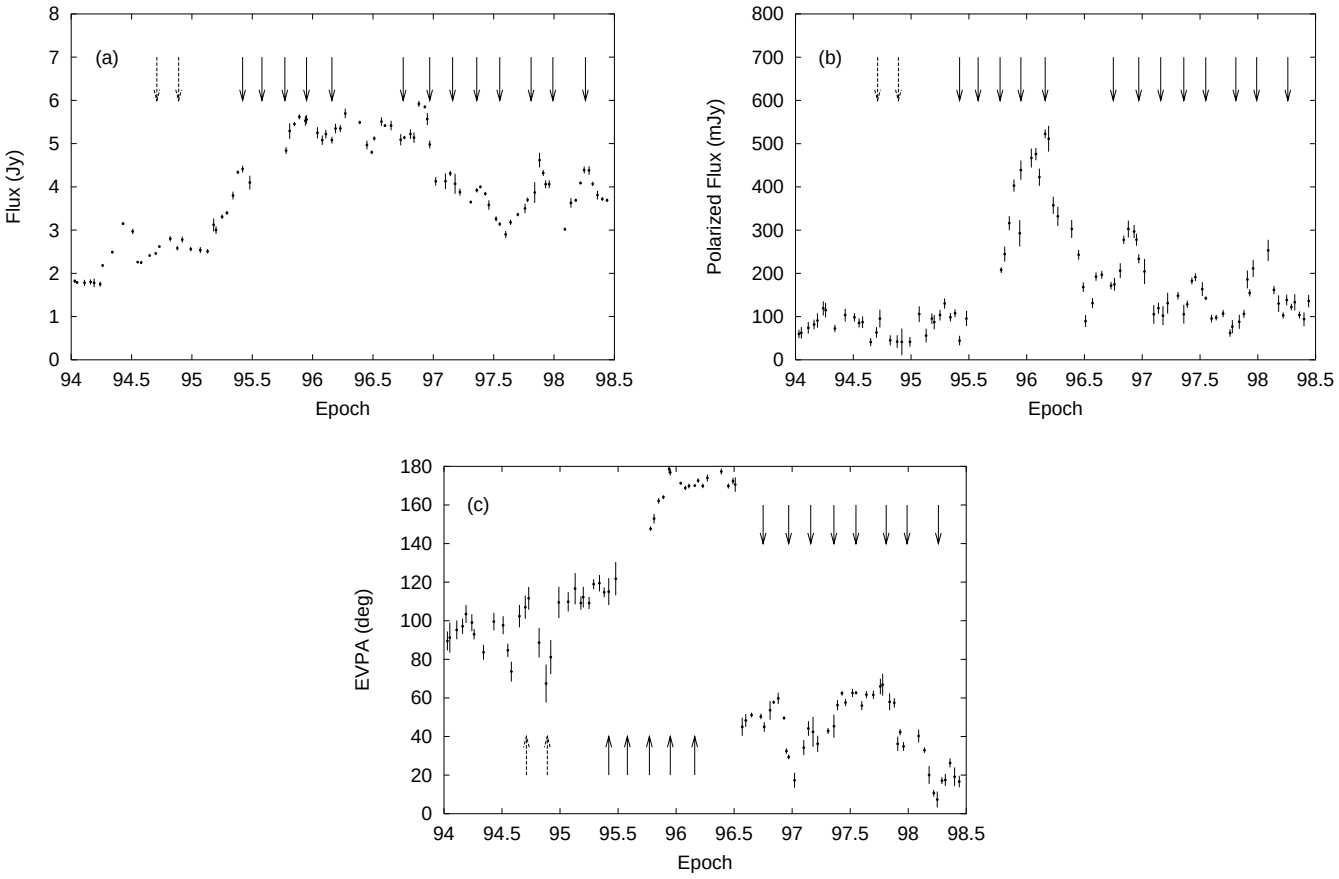

FIG. 1.—BL Lac (*a*) total flux, (*b*) percent linear polarization, and (*c*) polarization position angle at 14.5 GHz measured at the University of Michigan Radio Astronomy Observatory. Arrows indicate epochs of VLBI observations.

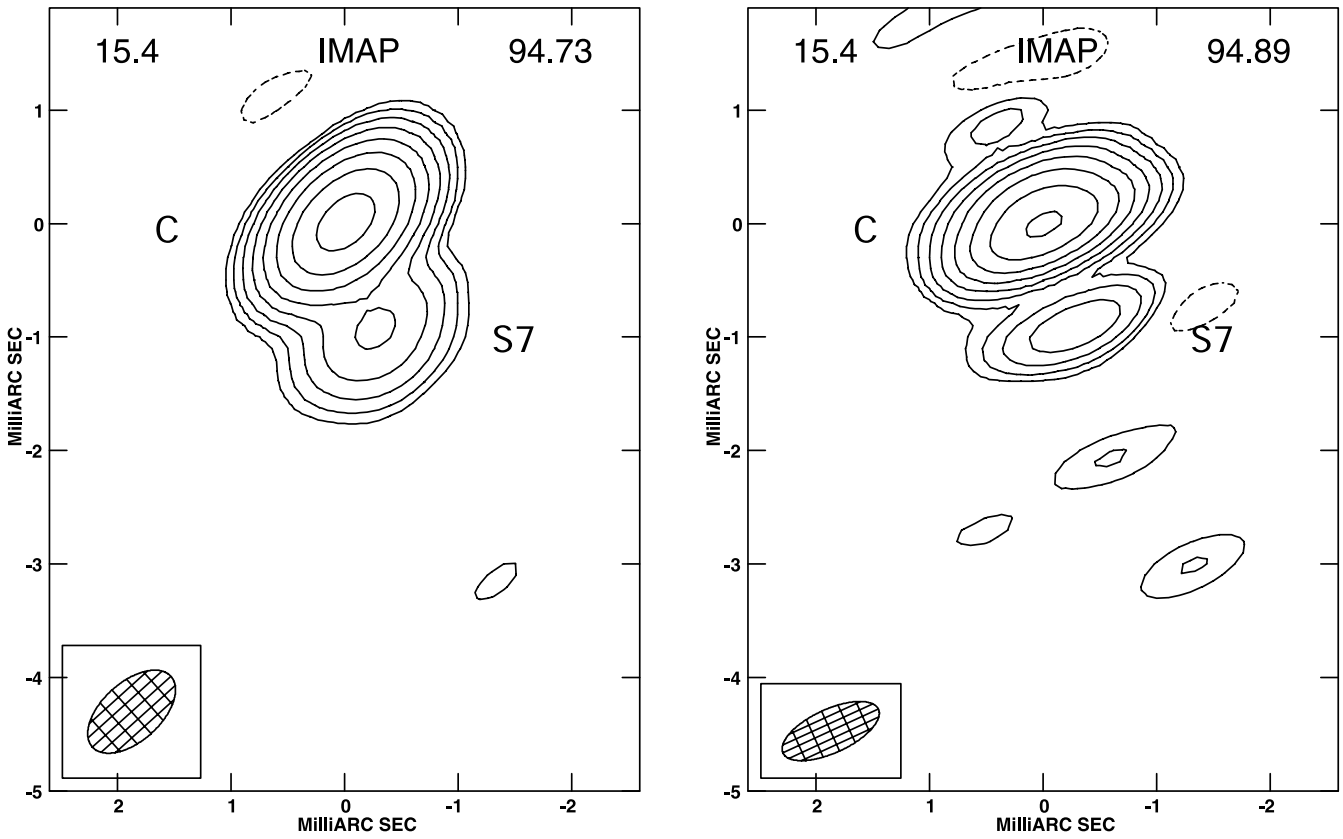

FIG. 2.—Total intensity maps of BL Lac at epochs 1994.73 and 1994.89 at 15.4 GHz. The contour levels are −10, 10, 20, 40, 80, 160, 320, and 640 mJy beam^{-1}.

was done with Difmap (Shepherd 1997) and the Astronomical Imaging Processing System (AIPS).

2.2. *VLBA Full Polarization Observations (1995.42–1998.28)*

The VLBA began support of full polarization VLBI observations starting in late 1994. We began a multifrequency, full polarization monitoring program soon afterward. The primary objective of this program was to obtain spectral and linear polarization information on the rapidly evolving parsec-scale structure of BL Lac for the first time. Based on previous VLBI observations (Mutel et al. 1990), we knew that the lifetime of typical superluminal component was at most a few years before fading below the detection limit of VLB maps. Therefore, frequent time sampling was essential to follow the evolution of each com-

TABLE 1

LOG OF OBSERVATIONS

Epoch	Telescopes[a]	Frequency (GHz)	Comments
1994.73.....	Seven-element VLBA	8.4, 15.4	Mk II, no polarization
1994.89.....	Seven-element VLBA, B	8.4, 15.4	B 8.4 GHz only; Mk II no polarization
1995.42.....	VLBA	8.4, 15.4, 22.2	
1995.58.....	VLBA	8.4, 15.4, 22.2	
1995.77.....	VLBA	15.4, 22.2	
1995.97.....	VLBA	15.4, 22.2	
1996.16.....	VLBA	15.4, 22.2	
1996.75.....	VLBA	15.4, 22.2, 43.2	
1996.95.....	VLBA	15.4, 22.2, 43.2	
1997.16.....	VLBA	15.4, 22.2, 43.2	No Kp, Mk (weather)
1997.36.....	VLBA	15.4, 22.2, 43.2	
1997.55.....	VLBA	15.4, 22.2, 43.2	Bad weather, high system temp. at 7 mm
1997.58.....	VLBA	43.2	
1997.62.....	VLBA	43.2	
1997.78.....	VLBA	15.4, 22.2, 43.2	Bad weather, no 43.2 GHz maps
1997.99.....	VLBA	15.4, 22.2, 43.2	Bad weather, no 43.2 GHz maps
1998.21.....	VLBA	15.4, 22.2, 43.2	

[a] Telescope codes: *B* Bonn, FRG 100 m; VLBA 10 × 25 m Full VLBA.

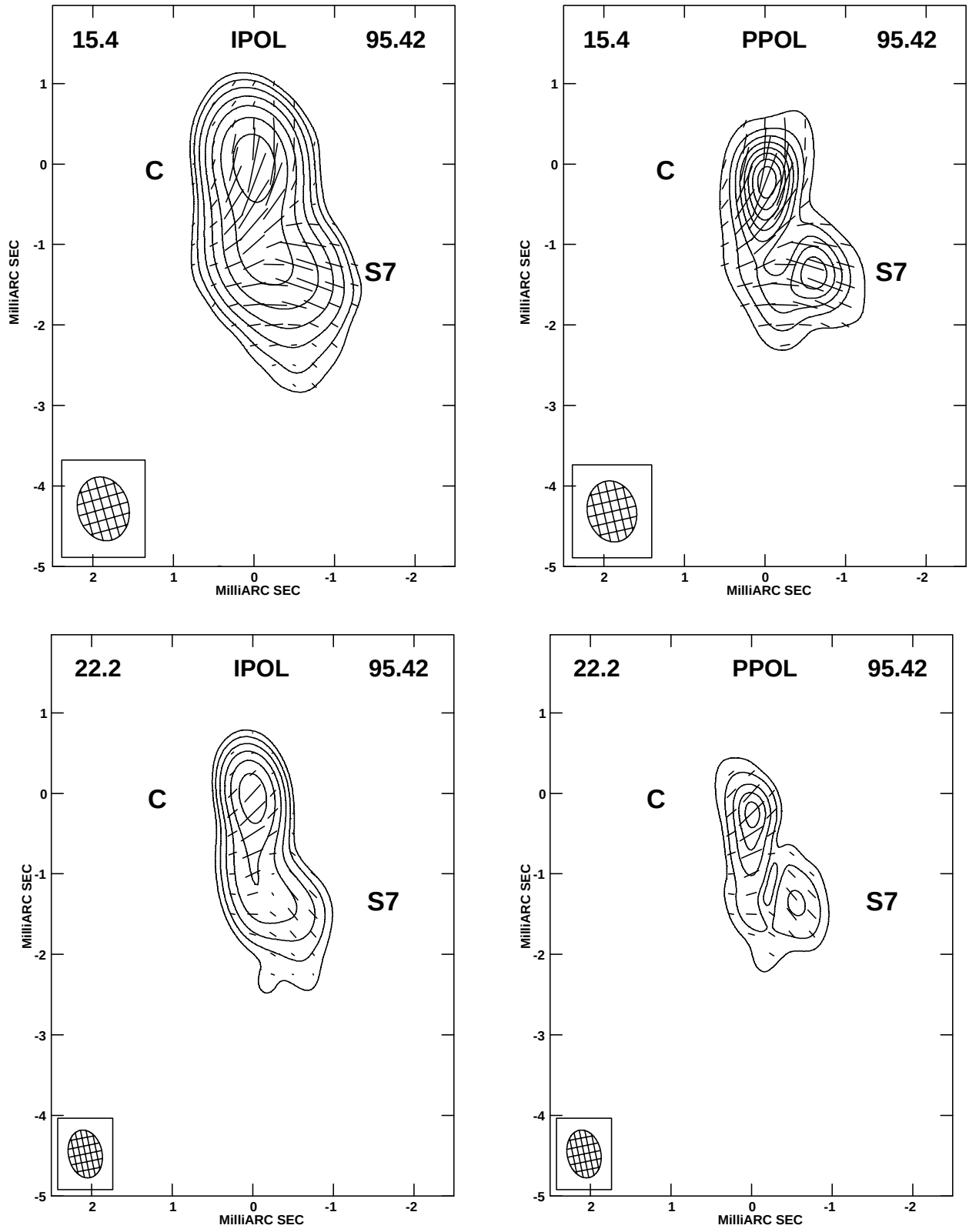

FIG. 3.—Maps of BL Lac in Stokes I and total linear polarization at 15.4 and 22.2 GHz at epoch 1995.42. *Top*: Contour levels for Stokes I (IPOL) maps are -15, 15, 30, 60, 120, 240, 480, and 960 mJy beam^{-1}. Contours for polarized intensity $(Q^2 + U^2)^{1/2}$ maps (PPOL) are 7.5, 15, 22.5, 30, 37.5, 45, and 52.5 mJy beam^{-1}. *Bottom*: Contour levels for Stokes I (IPOL) maps are -15, 15, 30, 60, 120, 240, and 480 mJy beam^{-1}. Contours for polarized intensity $(Q^2 + U^2)^{1/2}$ maps (PPOL) are 3.75, 7.5, 15, 22.5, and 30 mJy beam^{-1}.

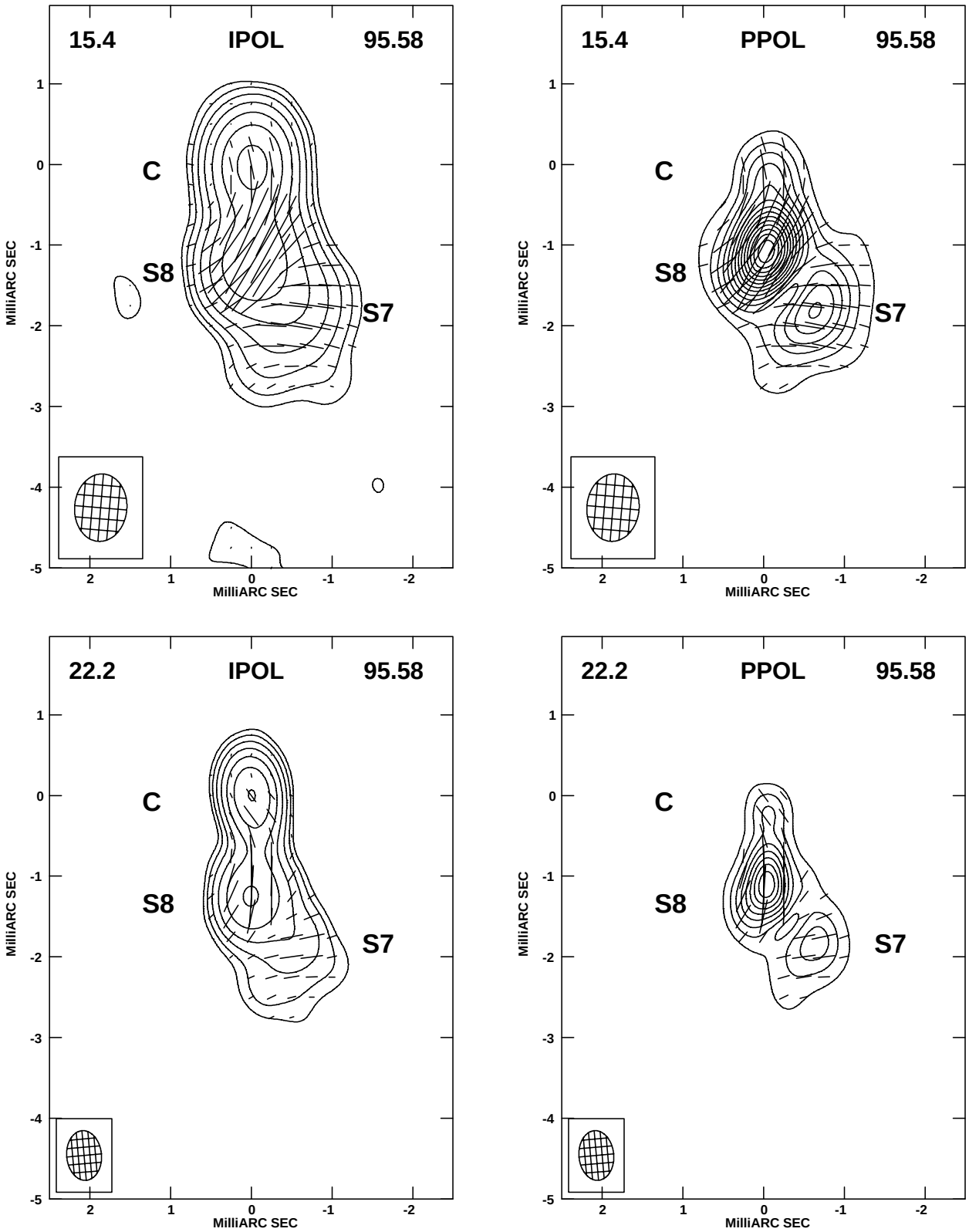

FIG. 4.—Maps of BL Lac in Stokes I and total linear polarization at 15.4 and 22.2 GHz at epoch 1995.58. Contour levels for Stokes I (IPOL) maps are -15, 15, 30, 60, 120, 240, 480, and 960 mJy beam^{-1}. Contours for polarized intensity $(Q^2 + U^2)^{1/2}$ maps (PPOL) are 7.5, 15, 22.5, 30, 37.5, 45, 52.5, 60, 67.5, 75, 82.5, 90, and 97.5 mJy beam^{-1}.

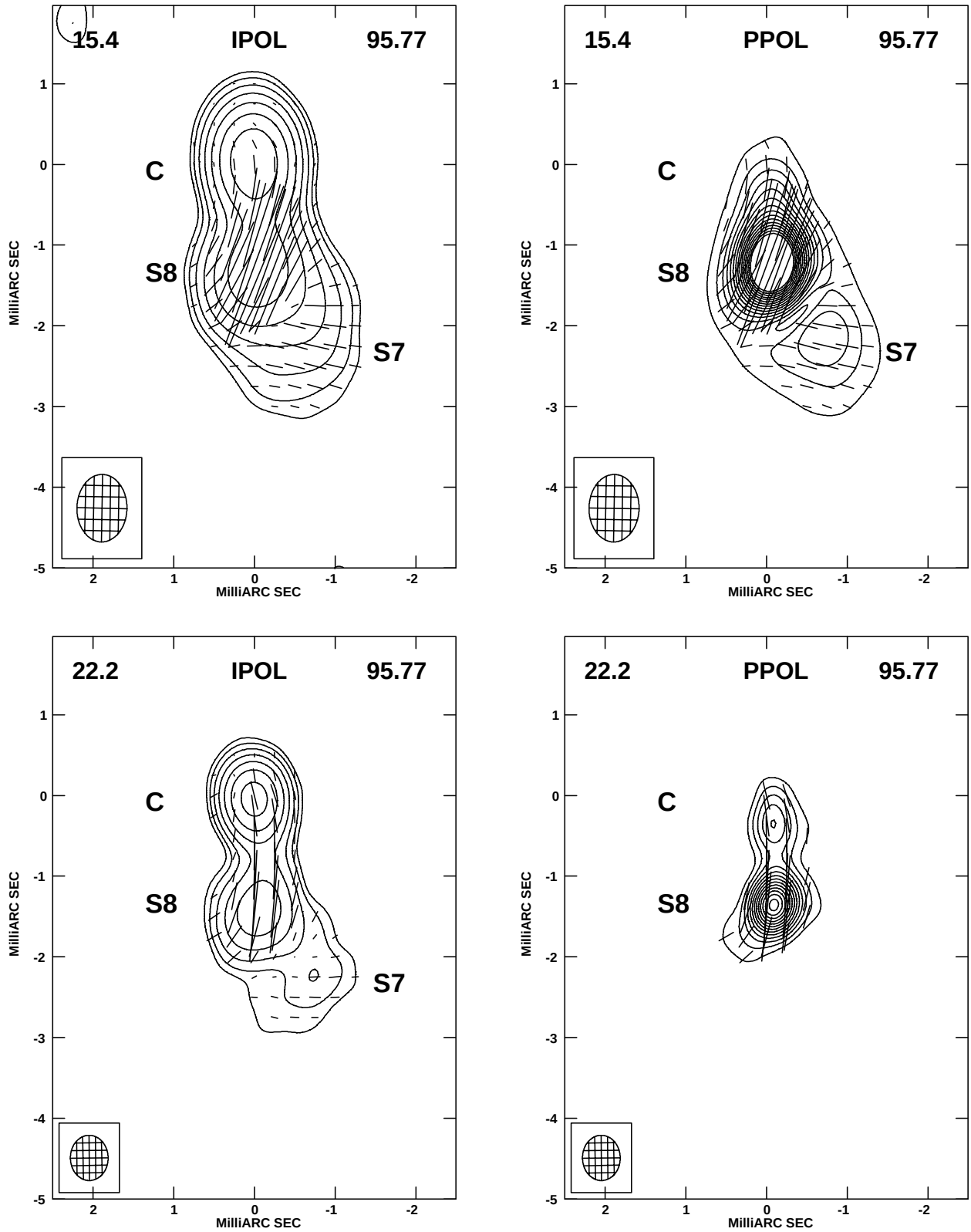

FIG. 5.—Maps of BL Lac in Stokes I and total linear polarization at 15.4 and 22.2 GHz at epoch 1995.77. Contour levels for Stokes I (IPOL) maps are -15, 15, 30, 60, 120, 240, 480, and 960 mJy beam^{-1}. Contours for polarized intensity $(Q^2 + U^2)^{1/2}$ maps (PPOL) are 7.5 (15.4 GHz only), 15, 22.5, 30, 37.5, 45, 52.5, 60, 67.5, 75, 82.5, 90, and 97.5 mJy beam^{-1}.

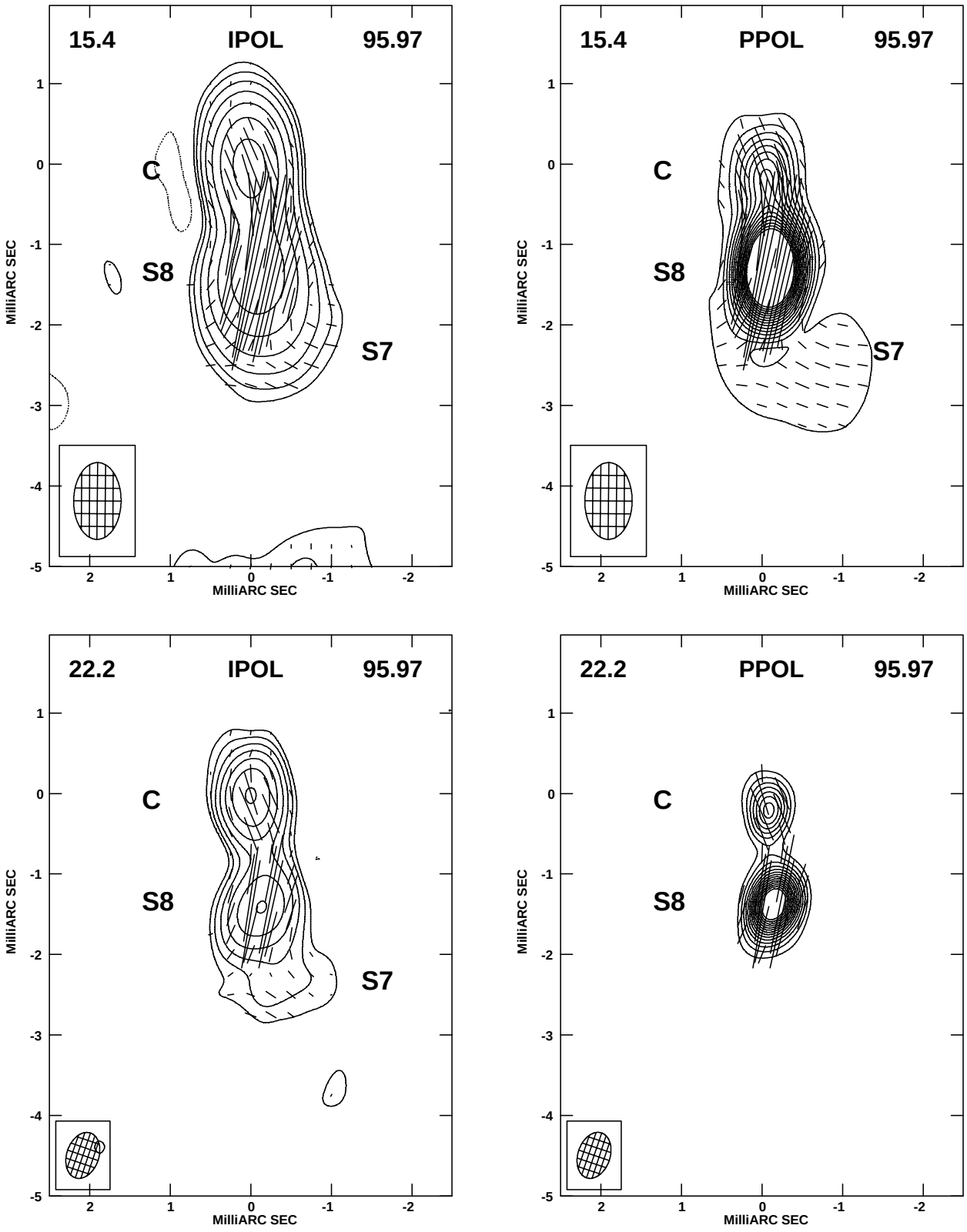

FIG. 6.—Maps of BL Lac in Stokes I and total linear polarization at 15.4 and 22.2 GHz at epoch 1995.97. Contour levels for Stokes I (IPOL) maps are -15, 15, 30, 60, 120, 240, 480, and 960 mJy beam^{-1}. Contours for polarized intensity $(Q^2 + U^2)^{1/2}$ maps (PPOL) are 7.5, 15, 22.5, 30, 37.5, 45, 52.5, 60, 67.5, 75, 82.5, 90, and 97.5 mJy beam^{-1}.

TABLE 2

COMPONENT TOTAL FLUX (S), POLARIZED FLUX (P), FRACTIONAL LINEAR POLARIZATION (m_L), CORE DISTANCE (r_c), POSITION ANGLE (ϕ_c), AND POLARIZATION POSITION ANGLE (χ_{pol})

Epoch (yr)	S (Jy)	P (mJy)	m_L	r_c (mas)	ϕ_c (deg)	χ_{pol} (deg)	Epoch (yr)	S (Jy)	P (mJy)	m_L	r_c (mas)	ϕ_c (deg)	χ_{pol} (deg)
	S7 S8							S7 S8					
1994.73.....	0.2	...	...	0.9	195	...	1994.73.....	...	...	...	...	...	...
1994.89.....	0.1	...	...	0.9	193	...	1994.89.....	...	...	...	...	...	...
1995.42.....	0.7	68	0.15	1.4	201	75	1995.42.....	...	...	...	...	...	...
1995.58.....	0.6	66	0.20	1.8	201	85	1995.58.....	1.1	140	0.08	1.0	183	148
1995.77.....	0.3	45	0.15	2.3	199	85	1995.77.....	1.2	136	0.16	1.2	185	163
1995.97.....	...	...	...	2.5	195	80	1995.97.....	1.8	247	0.14	1.3	185	168
1996.16.....	...	...	...	...	...	...	1996.16.....	1.8	382	0.13	1.6	188	165
1996.75.....	...	...	...	...	...	...	1996.75.....	1.7	139	0.09	1.8	192	17
1996.95.....	...	...	...	...	...	...	1996.95.....	0.9	117	0.25	2.0	192	30
1997.16.....	...	...	...	...	...	...	1997.16.....	1.0	23	...	2.2	184	178
	S9 S10							S9 S10					
1996.75.....	(0.9)	65	0.10	0.9	217	55	1996.75.....	...	...	...	0.1	225	...
1996.95.....	0.6	43	0.16	1.1	202	70	1996.95.....	...	...	...	0.2	201	...
1997.16.....	0.8	28	...	1.4	205	50	1997.16.....	...	...	...	0.4	206	...
1997.36.....	0.7	110	0.20	2.0	191	35	1997.36.....	...	...	...	0.5	202	...
1998.28.....	...	...	...	...	...	...	1998.28.....	1.8	44	0.08	1.7	190	15

NOTE.—Fluxes have been measured from the 15 GHz maps and positions from the 22 and 43 GHz maps.

TABLE 3

HELICAL PARAMETERS FOR COMPONENTS S7–S10

Component	Ψ (deg)	Θ (deg)	λ_1 (pc)	ϕ_1 (deg)	R_0 (pc)	z_1 (pc)	ξ (deg)	γ
S7	2.2 ± 0.1	8.0 ± 0.8	5.0 ± 0.2	200 ± 4	0.10 ± 0.01	0.09	182.0 ± 2.0	4.2
S8	1.8 ± 0.1	9.0 ± 0.7	1.5 ± 0.1	150 ± 6	0.05 ± 0.01	0.09	182.0 ± 4.4	3.0
S9	2.4 ± 0.1	8.5 ± 2.5	8.1 ± 0.5	90 ± 6	0.10 ± 0.01	0.09	182.0 ± 2.0	6.1
S10	2.2 ± 0.1	10.0 ± 0.3	9.0 ± 0.1	60 ± 2	0.10 ± 0.01	0.09	182.0 ± 0.5	3.6

ponent. We observed BL Lac at 15 epochs from 1995.42 to 1998.28, with a spacing of approximately two months between observations (but with some gaps caused by reproposing and scheduling; see Table 1). We initially chose observing frequencies of 8.4, 15.4 and 22.2 GHz but found that the improved angular resolution at the higher frequencies was a better match to the source structure. Hence, we replaced the 8.4 GHz observations with 43 GHz observations starting in late 1996. Figure 1 shows the 14.5 GHz flux, polarized flux, and polarization angle from the University of Michigan Radio Astronomy Observatory (UMRAO) with the epochs of our observations marked.

TABLE 4

THE ALLOWED RANGE OF COMPRESSION k AND VIEWING ANGLE θ FOR THE RELATIVISTIC SHOCK MODEL

Shock (1)	$\overline{m}$ (2)	I_d/I_u (3)	k (4)	θ (5)	k_{con} (6)
S7 forward	0.11	>2	0.6–0.8	4–6, 14	0.7–0.8
S7 reverse	0.11	>4	0.5–0.7	0.5, 9–12	0.5–0.7
S8 forward	0.12	>2	0–0.8	4–12, 22	0.4–0.7
S8 reverse	0.12	>100	0–0.7	1, 23	None
S9 forward	0.23	>8	0.0–0.4	3–5, 9	0.0–0.4
S9 reverse	0.23	>100	0–0.4	1, 7	0.0–0.5
S10 forward.....	0.10	>8	0–0.6	4–6, 17	0.5
S10 reverse.....	0.10	>8	0–0.6	1, 13–15	None

NOTE.—The parameter k_{con} is the compression with the viewing angle constrained by the helical model.

The data were correlated with the VLBA correlator at the Array Operations Center in Socorro, NM. Fringe fitting and amplitude calibration were done using AIPS. To solve for the instrumental polarization, we followed the reduction scheme described by Leppänen (1995) and more briefly in Leppänen et al. (1995). We summarize the calibration scheme below.

2.3. *Polarization Calibration*

Calibration of VLBP maps is similar to single-polarization VLB calibration, but with two important additions. In this section we briefly describe the calibration procedure we used for VLBA polarization maps. Full descriptions of VLB polarization calibration are given in Cotton (1993), Roberts, Wardle, & Brow (1994), and Leppänen et al. (1995).

2.3.1. *Instrumental Polarization*

The instrumental polarization of each telescope feed, i.e., the "D-terms" (Cotton 1993; Roberts et al. 1994) must be determined. This is most easily done by observing an unpolarized compact source over a large range of parallactic angle. Unfortunately, nearly all sources that are compact on milliarcsecond scales have measurable linear polarization.

Leppänen et al. (1995) describe an alternative method of solving for the feed parameters using polarized sources with

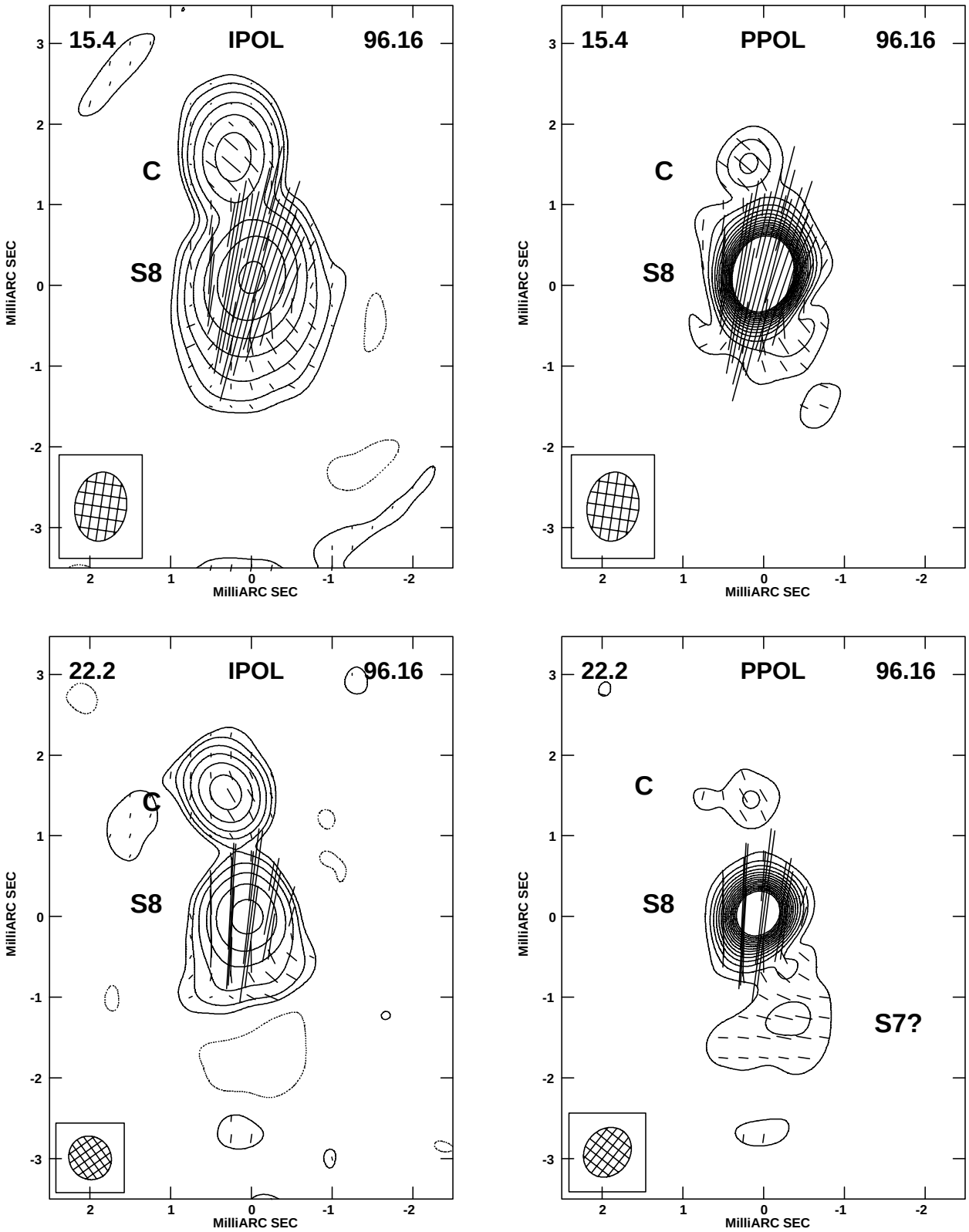

FIG. 7.—Maps of BL Lac in Stokes I and total linear polarization at 15.4 and 22.2 GHz at epoch 1996.16. Contour levels for Stokes I (IPOL) maps are -15, 15, 30, 60, 120, 240, 480, and 960 mJy beam^{-1}. Contours for polarized intensity $(Q^2 + U^2)^{1/2}$ maps (PPOL) are 7.5, 15, 22.5, 30, 37.5, 45, 52.5, 60, 67.5, 75, 82.5, 90, and 97.5 mJy beam^{-1}.

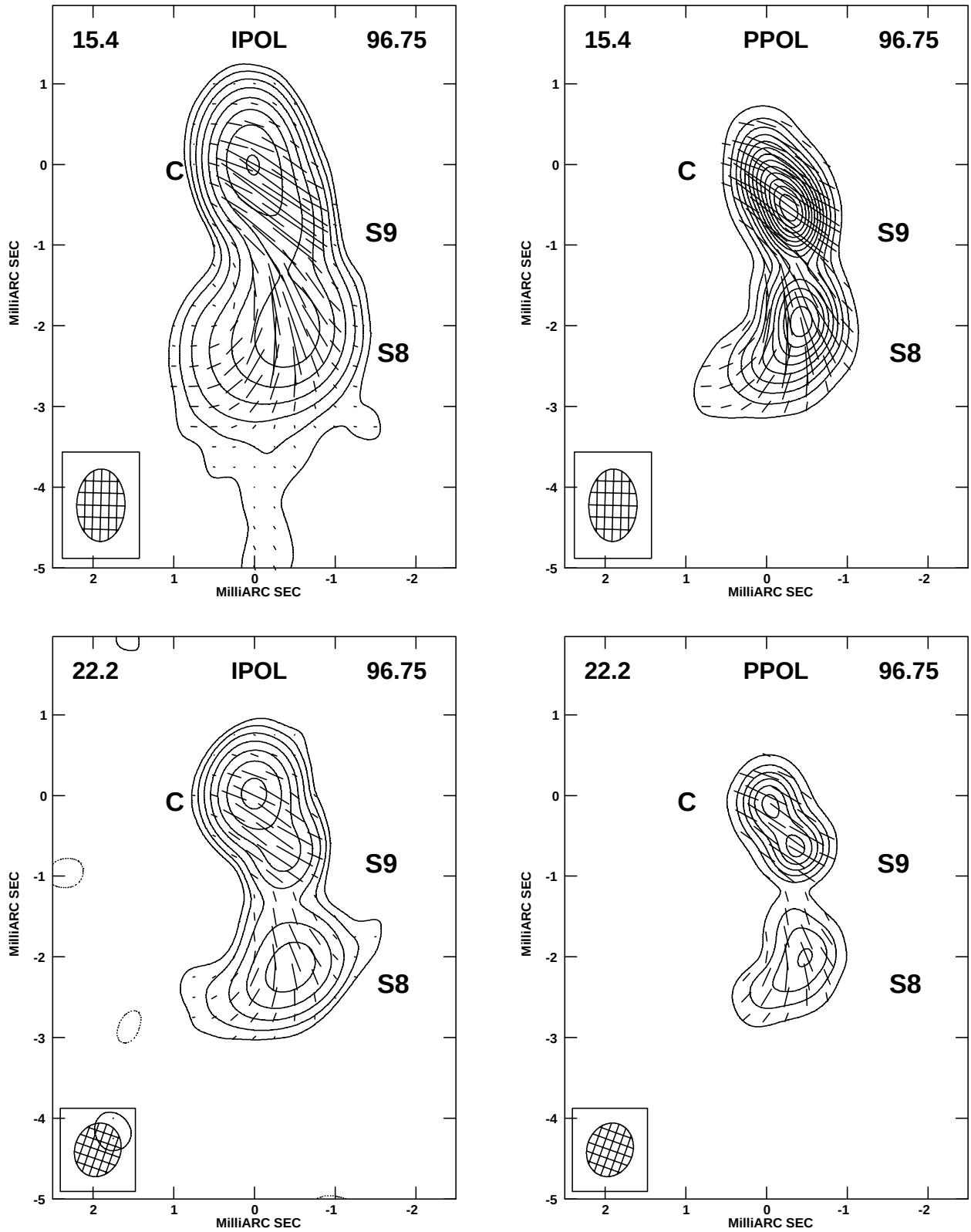

FIG. 8.—Maps of BL Lac in Stokes I and total linear polarization at 15.4, 22.2, and 43.2 GHz at epoch 1996.75. Contour levels for 15.4 and 22.2 GHz Stokes I (IPOL) maps are -15, 15, 30, 60, 120, 240, 480, 960, and 1920 mJy beam^{-1}. Contours for 43.2 GHz maps are -3.75, 3.75, 7.5, 15, 30, 60, 120, 240, and 480 mJy beam^{-1}. Contours for 15.4 and 22.2 GHz polarized intensity $(Q^2 + U^2)^{1/2}$ maps (PPOL) are 7.5, 15, 22.5, 30, 37.5, 45, 52.5, 60, 67.5, 75, 82.5, 90, and 97.5 mJy beam^{-1}. Contours for 43.2 GHz PPOL maps are 3.75, 7.5, and 15 mJy beam^{-1}.

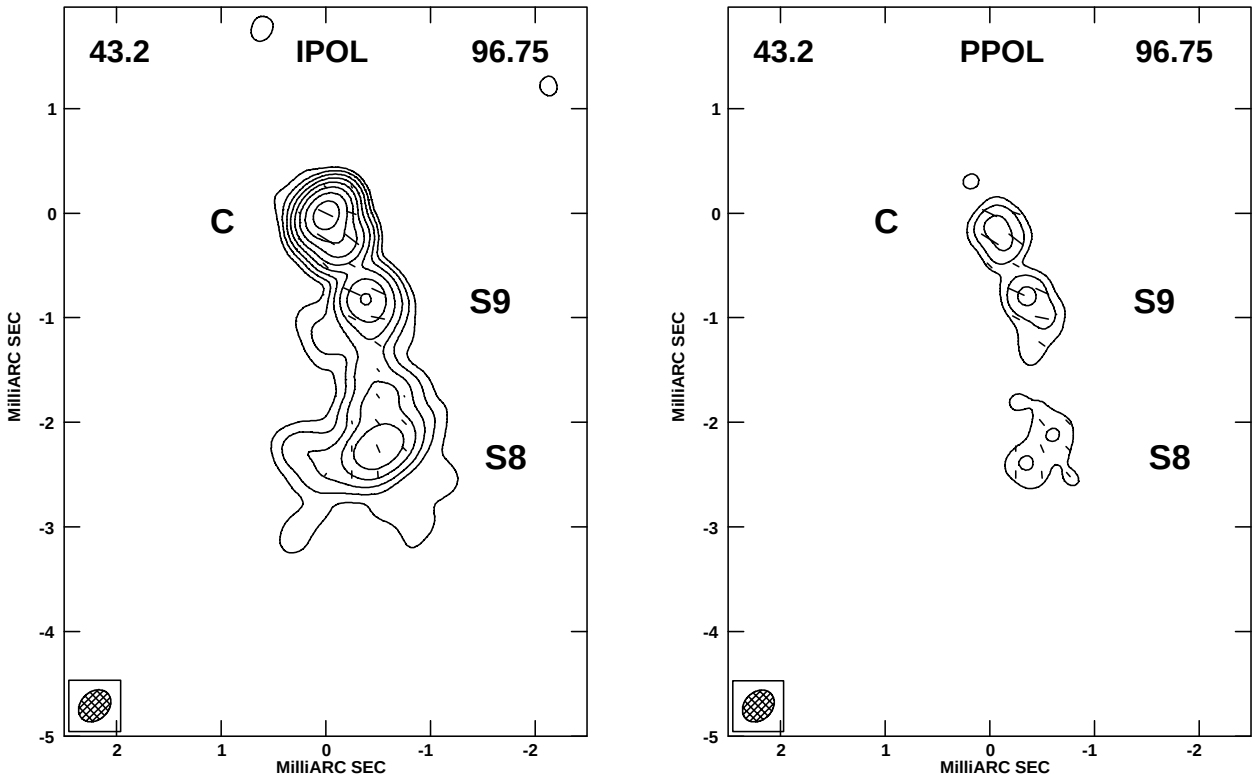

FIG. 8.—*Continued*

relatively simple structure. In this scheme, the target source itself may also be used as the calibrator for the instrumental polarization. The only requirement is that the source can be divided into a small number of subregions, each with constant Stokes parameters Q and U. The complex D-terms are determined by a least-squares fit to the observed cross-polarized visibilities. This algorithm, which is implemented in the AIPS program LPCAL, was used at all epochs. For most epochs, we computed independent D-term solutions using both BL Lac and an additional calibrator with adequate parallactic angle coverage (J0238+16 or J0423−01). For a typical set of complex D-term solutions at 15 GHz using BL Lac as the calibrator source, the average D-term magnitude is $\sim$0.025, with a few telescopes have D-term magnitudes as high as 0.05. The difference in independent D-term solutions using both BL Lac and J0238+16 as calibrator sources was small; the solutions agree within $\pm$0.005 rms, with the differences likely resulting from the imperfect subsource selection for BL Lac (Leppänen 1995). The D-term magnitudes obtained at 22.2 and 43.2 GHz are similar to those at 15 GHz and are also similar to those found by Leppänen et al. (1995) for 22 GHz observations taken in 1995. Although a few percent instrumental polarization for VLBA feeds is much smaller than many other telescope feeds used for VLBI (e.g., the EVN, Massi et al. 1997), it is comparable to the average fractional polarization of BL Lac and must be accurately measured and removed to ensure correct polarization maps.

2.3.2. *Absolute Linear Polarization Position Angle*

Since fringe fitting of the parallel hands (RR, LL) is done independently, there is an arbitrary phase offset $\Delta\phi$ between the RR and LL channels. This offset corresponds a position angle rotation $\Delta\chi = \frac{1}{2}\Delta\phi$ in the linear polarization vector. The offset appears to be stable over many hours for most telescopes used in VLB arrays (Roberts et al. 1994; Leppänen et al. 1995), so that a single phase correction can be applied at each epoch. This assumption was tested with data obtained at several epochs. We found that the R-L offset phase was stable within a few degrees.

In principle, the best technique for determining the absolute EVPA is to observe a linearly polarized compact source with known EVPA at the same observing frequency and epoch. This is the usual procedure at connected-element arrays such as the VLA, for which the compact source 3C 286 is often used for position angle calibration. At VLB resolutions, it is difficult to find compact sources with polarized components having stable position angles.

We initially tried to use the compact source J1803+784 as an EVPA calibrator, since historical data from the University of Michigan's Radio Astronomy Observatory (UMRAO) database indicated that the EVPA for this source was stable to slowly varying. However, starting in mid-1995 it underwent large, erratic changes in EVPA, rendering it useless as a calibrator. We therefore abandoned J1803+784 as an EVPA calibrator and instead decided to use the UMRAO data for BL Lac itself. This is generally not advisable since there is a possibility that highly polarized extended emission will contribute to the single dish polarization measurements. Indeed, an 18 cm map of BL Lac shows faint extended emission at least 100 mas to the southeast (Polatidis et al. 1995). However, a comparison of VLA maps (which show no extended emission at the 2000:1 scale) and the shortest VLBI baselines indicate that even if the extended emission were completely polarized, there would only be a contribution of $\sim$5% to the total polarized flux, giving a maximum deviation of the net polarization angle of $\sim 3^\circ$.

We calibrated the BL Lac EVPA by summing clean components from the 14.5 GHz Stokes Q and U maps and com-

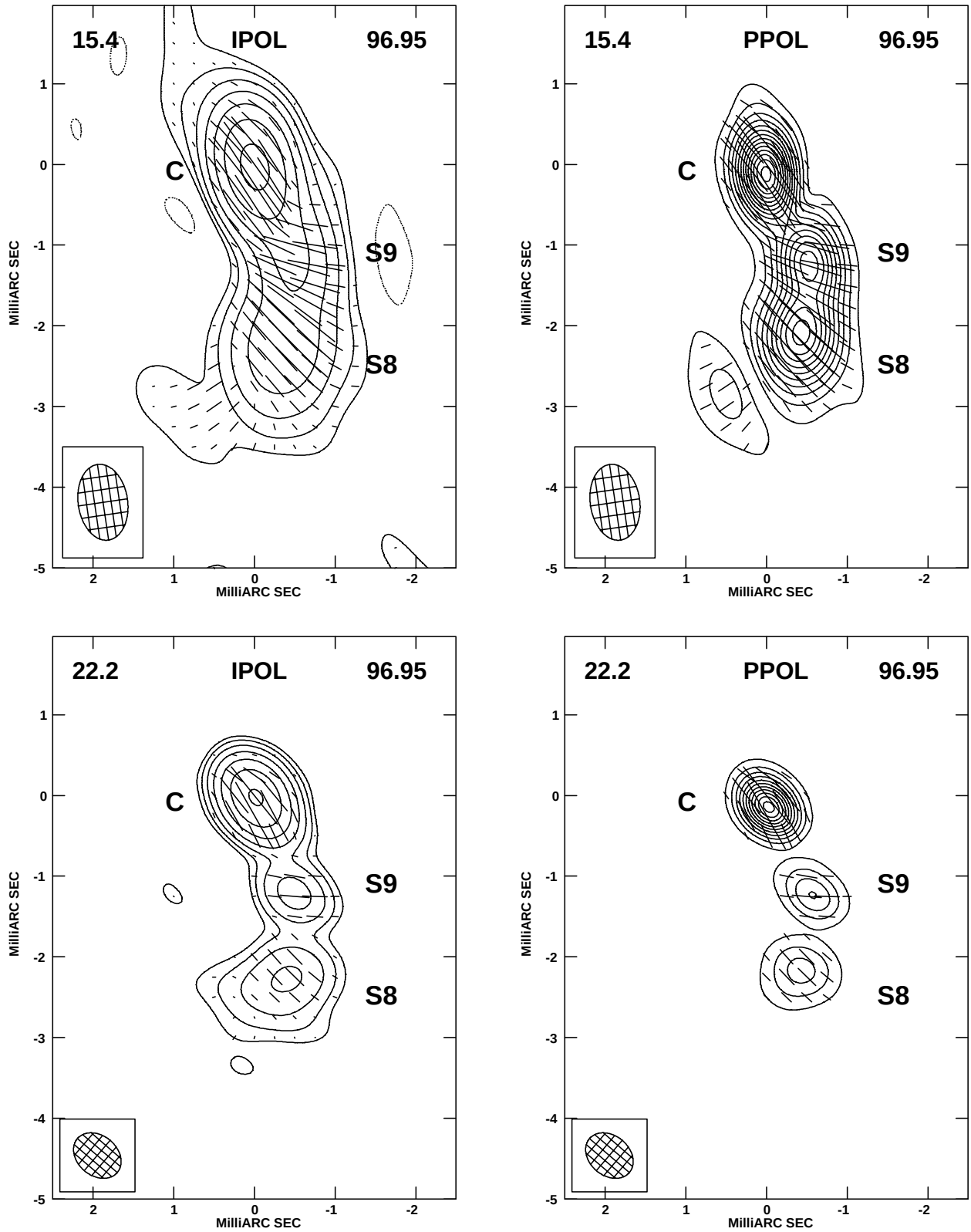

FIG. 9.—Maps of BL Lac in Stokes I and total linear polarization at 15.4, 22.2, and 43.2 GHz at epoch 1996.95. Contour levels for 15.4 GHz Stokes I (IPOL) maps are -30, 30, 60, 120, 240, 480, 960, and 1920 mJy beam^{-1}. Contours for 15.4 GHz polarized intensity $(Q^2 + U^2)^{1/2}$ maps (PPOL) are 7.5, 15, 22.5, 30, 37.5, 45, 52.5, 60, 67.5, 75, 82.5, 90, and 97.5 mJy beam^{-1}. The 22 GHz IPOL maps have one extra contour level at ± 15 mJy beam^{-1}. Contour levels for the 43.2 GHz IPOL maps are -7.5, 7.5, 15, 30, 60, 120, and 240 mJy beam^{-1}; contours for the 43.2 GHz PPOL maps are 1.87, 3.75, 7.5, 15, and 22.5 mJy beam^{-1}.

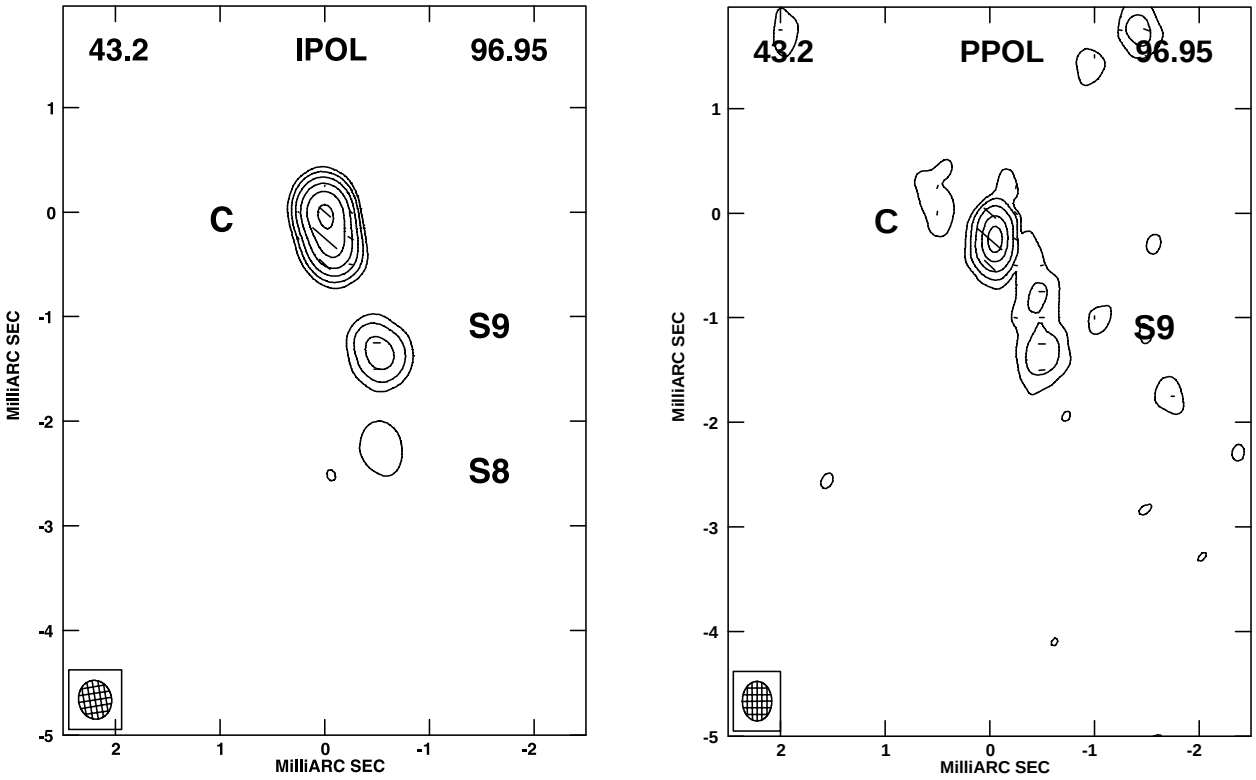

FIG. 9.—*Continued*

paring them with the UMRAO values at the same epoch as the VLBI observation. We then solved for the rotation angle required to force agreement with the UMRAO 15 GHz data. At 22 and 43 GHz, we were unable to use this method, as UMRAO does not observe at those frequencies. For several epochs, we also observed BL Lac and 3C 286 using the VLA at 22 and 43 GHz. We found that the EVPA at the higher frequencies was equal to the 14.5 GHz EVPA within measurement errors (typically $\pm 5°$) after correcting for the known rotation measure of BL Lac (RM $= -198$ rad m^{-2}, Rudnick et al. 1984). In addition, we used a third independent calibration check during the 1997 July observations. Taylor (1998) has recently suggested that component C4 of 3C 279, which has an EVPA $\sim 70°$ and low rotation measure, is a stable EVPA calibrator for VLBP observations at frequencies above 5 GHz. We observed 3C 279 and used this component to calibrate the 43.2 GHz maps at epochs 1997.58 and 1997.62. Our map from 2 weeks previous (1997.55) shows the components having nearly the same position angle, hence confirming the validity of the calibration scheme.

3. RESULTS

3.1. *1994 Maps*

The 15.4 GHz maps from epochs 1994.78 and 1994.89 are shown in Figure 2. The 8.4 GHz maps did not have sufficient angular resolution to distinguish components and are not shown. Both maps show a very similar core-knot structure, with no measurable change in core-knot separation in the 0.11 yr between observations. Gaussian model fits to each map resulted in separations of 0.93 ± 0.07 and 0.94 ± 0.06 mas for the two epochs. Hence, we find an upper limit for angular motion of 0.84 mas yr^{-1} or $\beta_{\rm app} \leq 2.7\ h^{-1}$. Based on maps from subsequent epochs we have identified the knot with component S7 (see next section).

3.2. *VLBA Maps (1995.47–1998.28)*

The VLBA monitoring campaign imaged BL Lac using full polarization mode at several frequencies over 15 epochs. Multifrequency total intensity and polarized intensity maps for 13 epochs are shown in Figures 3–15. In addition, a pair of 43 GHz maps separated by 2 weeks (epochs 1997.58, 1997.62) are shown in Figure 16. The image dynamic range at a given frequency varies considerably from epoch to epoch, particularly at the higher frequencies. This is a result of variable weather conditions and occasional equipment malfunctions. For several epochs it was impossible to produce useful images at 43 GHz due to high winds, heavy rain, or snow resulting in poor pointing and high opacity.

In the following subsections we discuss the trajectories, speeds, and polarization properties of both the core and knots as they evolve along the jet.

3.2.1. *Core Properties*

3.2.1.1. Angular Size, Brightness Temperature

The well-known core-jet morphology of BL Lac is evident in all maps. We have identified the core component (which we assume to be stationary) with the northernmost emission region in the total intensity maps. We have used its centroid (measured in the total intensity maps) as the fiducial origin for measuring the position of all other components. This is consistent with all previous VLB studies of this source, e.g., (Mutel et al. 1990; Tateyama et al. 1998).

The angular size of the core is difficult to establish since it is often blended with emerging jet components. In order to determine the core's intrinsic angular size and brightness temperature, we chose an epoch (1998.28) in which there was no evidence of emerging components. We fit an elliptical Gaussian model to the core using the AIPS task JMFIT. The deconvolved mean FWHM angular size at

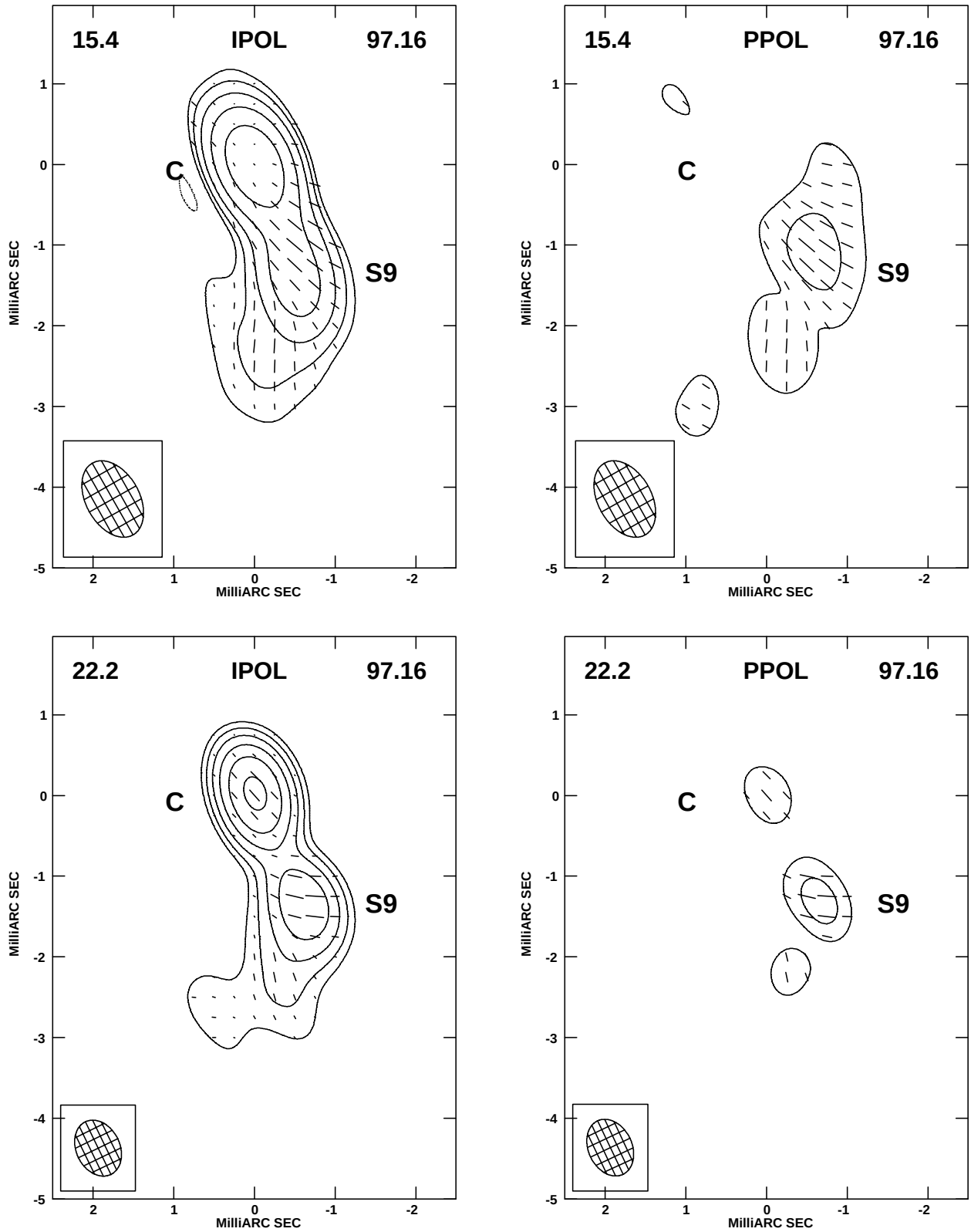

FIG. 10.—Maps of BL Lac in Stokes I and total linear polarization at 15.4, 22.2, and 43.2 GHz at epoch 1997.16. Contour levels for 15 GHz Stokes I (IPOL maps are -30, 30, 60, 120, 240, 480, and 960 mJy beam^{-1}. Contours for the 22.2 GHz IPOL map is -15, 15, 30, 60, 120, 240, and 480 mJy beam^{-1}. Contours for 15.4 and 22.2 GHz polarized intensity maps (PPOL) are 7.5 and 15 mJy beam^{-1}. Contours for 43.2 GHz maps are (IPOL) -15, 15, 30, 60, 120, 240, and 480 mJy beam^{-1} and (PPOL) 3.75 and 7 mJy beam^{-1}.

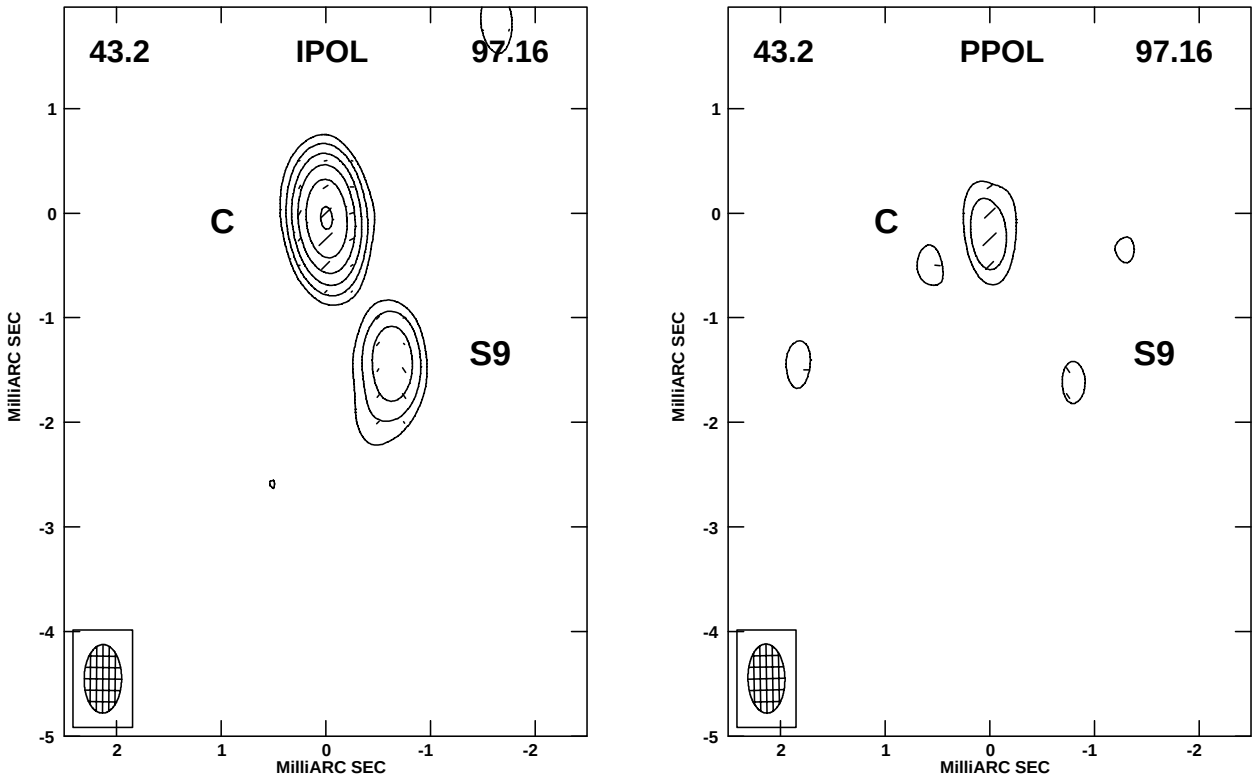

FIG. 10.—*Continued*

43 GHz was 0.08 ± 0.01 mas, compared with a resolving beam of 0.30×0.30 mas. The resulting brightness temperature is $T_B = 5.1 \times 10^{11}$K.

3.2.1.2. Core Polarization

The fractional polarization of the core is highly variable, both with epoch and frequency. The polarization ranges from very low (much less than 1%, e.g., 15 GHz epoch 1997.36) to $\sim$10% polarized (e.g., 15–43 GHz epoch 1996.95). Furthermore, the position of the core maximum in the polarized intensity map is sometimes offset from the peak in the total intensity. For example, comparison of the 15 GHz total and polarized intensity maps at epoch 1996.95 (Fig. 9) shows a small shift in the core position. The 22 and 43 GHz maps at the same epoch clarify the situation: the core is blended with a new, highly polarized component (S10, see below) which is just emerging. This is clearly seen in Figure 17, in which we have plotted one-dimensional profiles of all six maps along position angle 195°.

Figure 18 shows similar one-dimensional profiles at epoch 1997.36 when the core appears to have no blended components. The core polarization at 15 GHz is very low: inspection of the polarized intensity map resulted in an upper limit $p < 0.3\%$. At 22 GHz the fractional polarization is $p = 0.8 \pm 0.3\%$. At 43 GHz there is significant polarization structure (Fig. 11) with fractional polarization varying from 2%–5% with an average $p \sim 3\%$. Since the core is much less strongly depolarized at shorter wavelengths, it suggests depolarization by thermal plasma within the core or by a turbulent foreground Faraday screen. The latter is much more likely since it would be difficult to sustain thermal gas within the relativistic jet itself.

3.2.1.3. Frequency Dependence of Core-Knot Separation

The core emission is thought to result from a synchrotron self-absorbed, optically thick source. Since the observed core position corresponds to the region of one optical depth, the position will depend on observing frequency. For conical jet models, the optical depth decreases with distance from the vertex. If the knot position is frequency independent (e.g., optically thin) the core-knot separation at a given epoch will be frequency dependent, with increasing separation at lower frequencies.

Königl (1981) analyzed the expected frequency dependence and found that it scales as $\Delta r \propto \nu^{1/k_s}$ where k_s is a function of the jet's physical parameters (magnetic field, electron energy spectrum and density). For equipartition jets (equal particle and magnetic field energies), we expect $k_s \sim 1$.

Lobanov (1998) derives an expression for the expected core position shift between frequencies ν_1 and ν_2 assuming an equipartition jet with synchrotron luminosity $L_{\rm syn}$ as

$$\Delta r_{\rm mas} \approx \frac{C_r(1+z)}{D_L \gamma^2 \phi_0} \frac{\nu_2 - \nu_1}{\nu_2 \nu_1} \left[\frac{L_{\rm syn} \sin\theta}{\beta(1-\beta\cos\theta)\Theta_R} \right]^{2/3}, \quad (1)$$

with $C_r = 4.56 \times 10^{-12}$, D_L is the luminosity distance in pc, $\nu_{1,2}$ are the observing frequencies (Hz), $L_{\rm syn} = 2.3 \times 10^{41}$ ergs s^{-1}(taken directly from Lobonov 1998), ϕ_0 is the jet opening angle (radians), z is the redshift, and Θ_R is the log of the ratio of the jet to the initial nozzle radius ($\Theta_R \sim 5$).

We have measured the core-knot separation between the 22 and 43 GHz maps for the six epochs where we have adequate 43 GHz data (1996.75–1998.28). The predicted shift is too small to measure accurately ($\Delta r < 0.1$ mas), consistent with all observed separations within the uncertainty of each measurement.

3.2.2. *Jet Properties*

At most epochs there are either one or two polarized "knots" (or components) south of the core which appear to

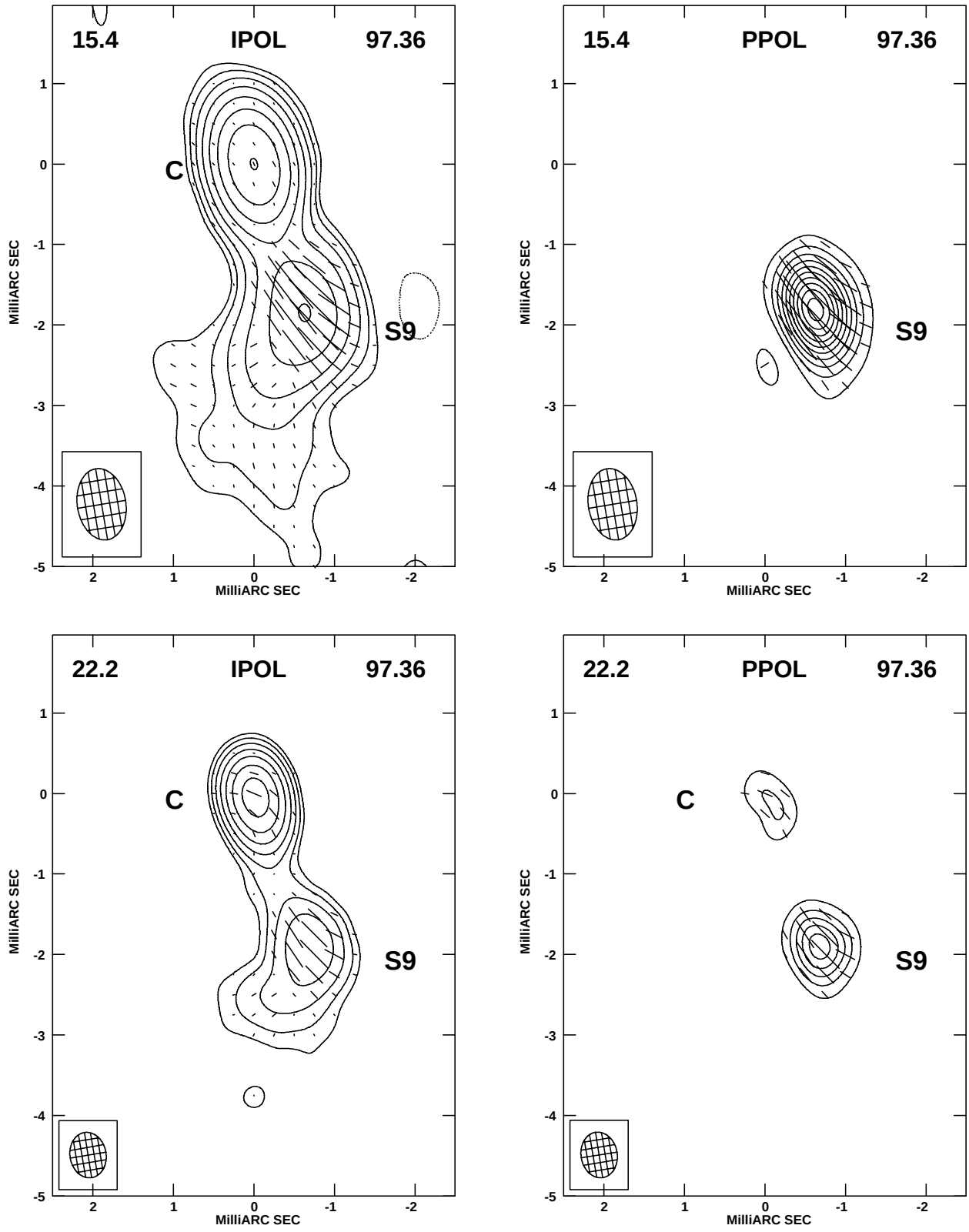

FIG. 11.—Maps of BL Lac in Stokes *I* and total linear polarization at 15.4, 22.2, and 43.2 GHz at epoch 1997.36. Contour levels for Stokes *I* (IPOL) maps are − 15, 15, 30, 60, 120, 240, 480, and 960 mJy beam^{-1}. Contours for 15.4 and 22.2 GHz polarized intensity maps (PPOL) are 7.5, 15, 22.5, 30, 37.5, 45, 52.5, 60, 67.5, 75, 82.5, 90, and 97.5 mJy beam^{-1}. Contours for 43.2 GHz PPOL maps are 3.75, 7.5, and 15 mJy beam^{-1}.

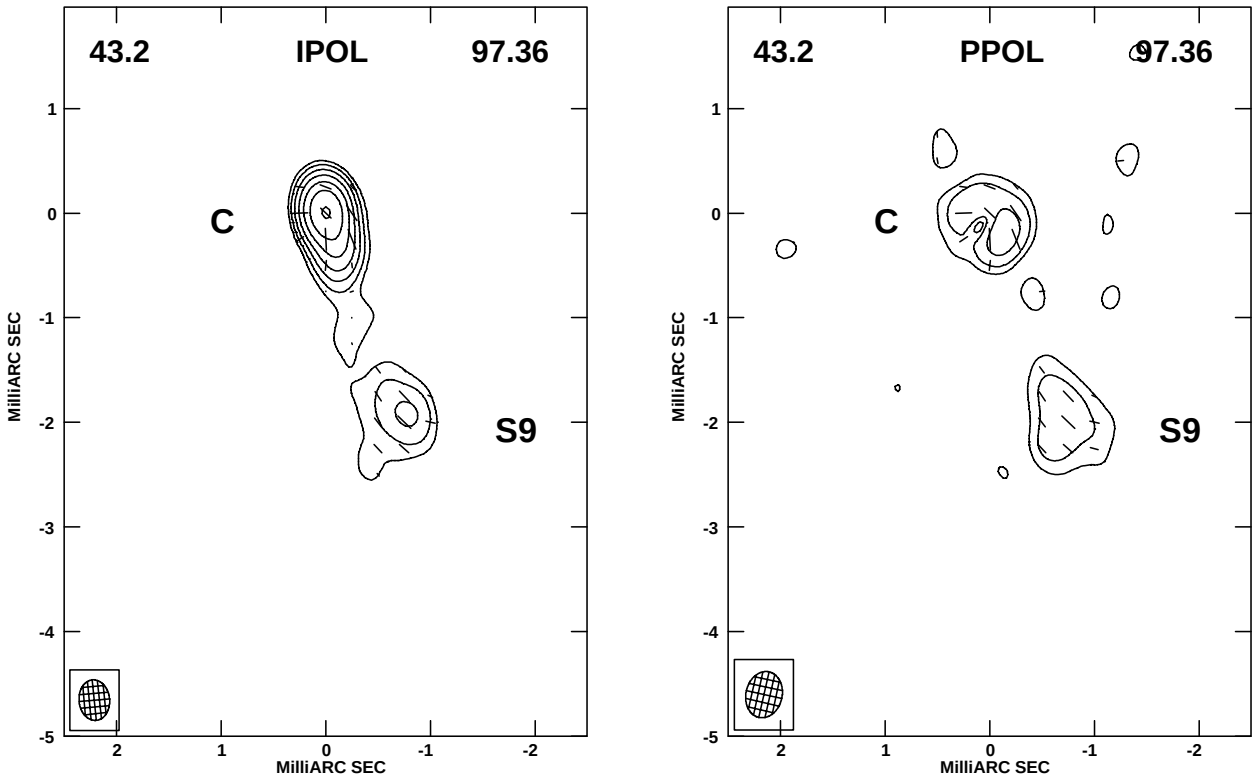

FIG. 11.—*Continued*

move along position angle ~185°–200° depending on the epoch and distance from the core. By comparing maps made at closely spaced epochs, we have identified four components (denoted S7–S10), all of which are moving superluminally.

Close inspection of the total versus polarized intensity maps at each epoch shows that jet components can be identified more clearly in the polarized intensity maps. A good example is the pair of 15 GHz maps at epoch 1996.95 (Fig. 9). Although the *polarized* map shows two distinct knots quite clearly (as do the 22 and 43 GHz maps), the 15 GHz *total* intensity map shows only a smoothly bent jet. Table 2 lists positions, angular sizes, and polarization angles for components S7–S10. The size and position measurements were obtained by fitting elliptical Gaussians to each component using the AIPS task JMFIT.

3.2.2.1. Spectral Index

Spectral index maps matching the available frequencies were made using maps at all three frequencies, restored with the largest (15 GHz) restoring beam. Because nascent components were often blended with the core at lower frequencies, aligning the maps accurately was difficult. Therefore, we only analyzed those epochs for which the core was well separated from superluminal components. Figure 19*a* shows one-dimensional slices through the 15, 22, and 43 GHz maps for epoch 1997.36. Figure 19*b* shows the spectral indices computed from these one-dimensional slices. The spectral index of the core is nearly zero while that of component S9 is negative ($-0.5 < \alpha_{S9} < -0.7$), although there is a large uncertainty in spectral index since we could not sample each frequency using scaled (u, v) arrays. This means that the angular resolution of maps at each frequency was quite different, so that frequency-dependent component size effects could substantially alter the measured fluxes, and hence the spectral index.

3.2.2.2. Component Trajectories and Speeds

Figures 20, 21, 22, and 23 show the trajectories of components S7–S10 for all epochs along with a best-fit helical trajectory (see § 4.1). All four trajectories are clearly bent and nonradial. Figure 24*a* shows the core-component radial separation of components S7–S10 versus epoch along with a least-squares linear fit. with apparent speeds $\beta_a = (3.7 \pm 0.4)\ h^{-1}$, $(2.2 \pm 0.1)\ h^{-1}$, $(5.0 \pm 0.2)\ h^{-1}$, and $(3.7 \pm 0.3)\ h^{-1}$ for S7–S10, respectively. By extrapolating the linear fits to zero core-component distance, the "birth" epochs are $t_0 = 1994.12 \pm 013$, 1994.20 ± 0.05, 1996.24 ± 0.05, and 1996.87 ± 0.06. The linear approximation is satisfactory for all components except S10, which had a somewhat slower speed during the first year ($3.0 \pm 0.3\ h^{-1}$). Evidently, the component pairs (S7, S8) and (S9, S10) were each ejected from the core at nearly the same epoch, although with different speeds. In both pairs there is a slow (S8; S10) and a fast (S7; S9) component. To our knowledge, this phenomenon has not been previously reported for any other superluminal source.

3.2.2.3. Component Polarization

Table 2 lists the fractional polarization and EVPAs for all four components as a function of core distance. The EVPAs of all four components are initially randomly oriented with respect to the jet axis (Fig. 27). As components S8, S9, and S10 evolve, the EVPA rotates within 20° of the assumed jet direction, consistent with a transverse shock. On the other hand, component S7's EVPA rotates nearly perpendicular to the jet axis, indicating that the magnetic field of the emitting region is parallel to the jet axis. It is clear that none

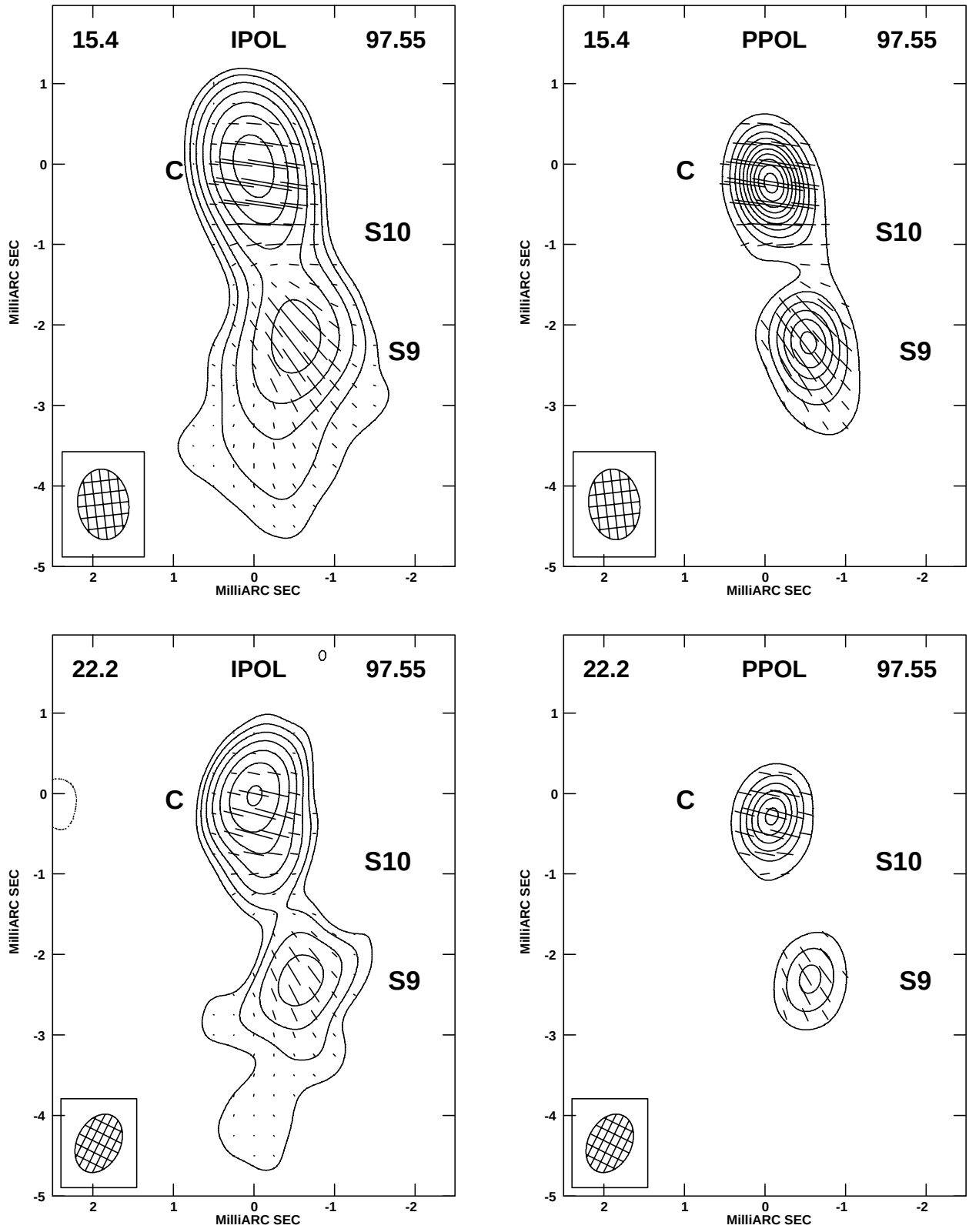

FIG. 12.—Maps of BL Lac in Stokes *I* and total linear polarization at 15.4, 22.2, and 43.2 GHz at epoch 1997.55. Contour levels for 15.4 and 22.2 GHz Stokes *I* (IPOL) maps are -15, 15, 30, 60, 120, 240, 480, and 960 mJy beam^{-1}. Contours for 15.4 and 22.2 GHz polarized intensity maps (PPOL) are 7.5, 15, 22.5, 30, 37.5, 45, 52.5, 60, 67.5, 75, 82.5, 90, and 97.5 mJy beam^{-1}. Contour levels for 43.2 GHz maps are (IPOL) -7.5, 7.5, 15, 30, 60, 120, 240, and 480 mJy beam^{-1} and (PPOL) 1.87, 3.75, 7.5, and 15 mJy beam^{-1}.

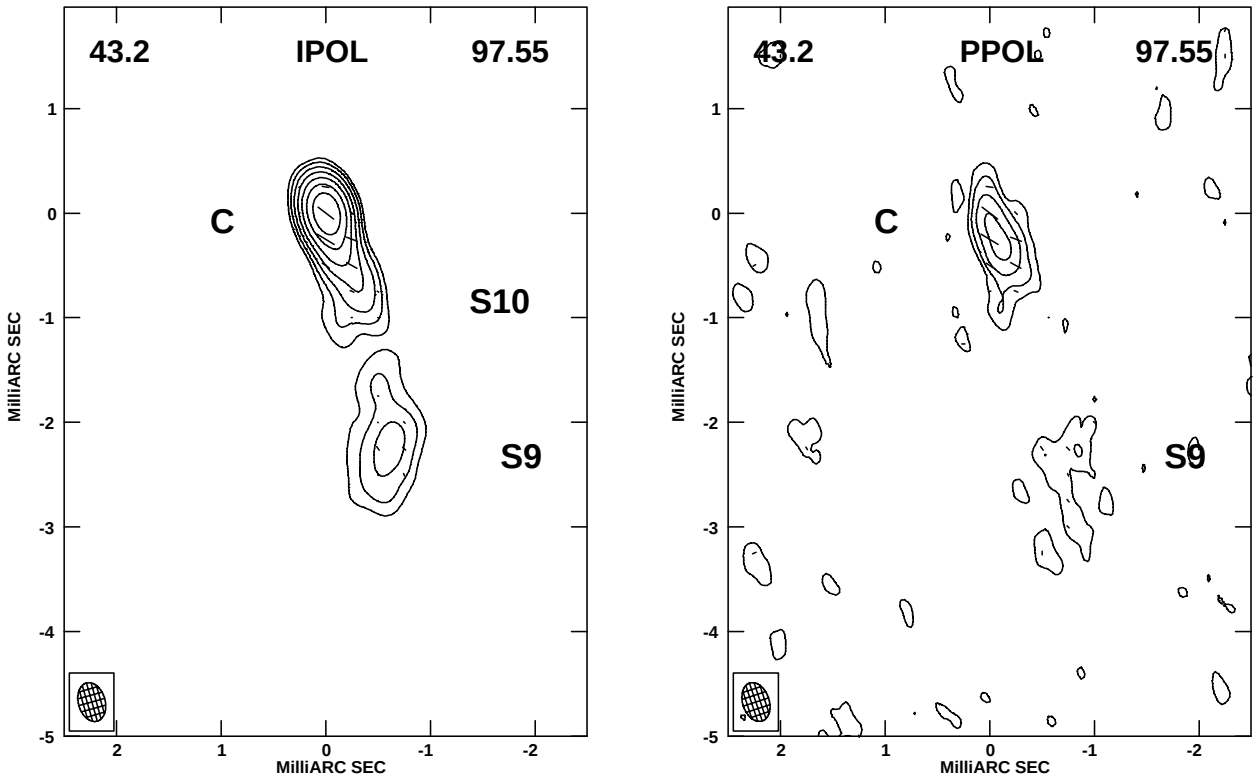

FIG. 12.—*Continued*

of the four components' observed EVPAs are consistent with models of plane-perpendicular shocks propagating along the jet flow direction, although this may be a useful approximation for some components as they evolve away from the core.

4. DISCUSSION

4.1. *Helical Geometrical Model*

Several lines of evidence indicate that the underlying jet in BL Lac has a curved or bent geometry. First, low frequency VLBI maps (Fig. 25) show faint decaparsec scale emission to the southeast at position angle $\sim 170°$ suggesting that the flow bends to the southeast from the parsec-scale position angle range 195°–205°. Parsec-scale maps at some epochs (e.g., 1996.95, 1997.36) also show weak emission bending toward the direction of the larger scale emission. The most convincing evidence is the nonradial motion of the shocks as discussed in § 3.2. If we assume the core is stationary, the trajectories cannot be rectilinear. Since a helical model has been successfully applied to the parsec-scale jets structure in several other AGNs (Mrk 501, Conway & Wrobel 1995; 3C 345, Steffen et al. 1995), we were motivated to apply this model to describe the shock trajectory, flux boost, and apparent speed for components observed in BL Lac.

We have applied the light adiabatic jet model of Hardee (1987) for the large-scale geometry of the jet flow. Shock components follow the flow, which is a helix mapped onto a conical surface. From the model we obtain the position, the apparent velocity, and the Doppler boost of a component as a function of position in the flow, and we compare them with the observations. We define the helical geometry using cylindrical coordinates (R, ϕ, z) with the helical axis along axis z.

The model makes the following simplifying assumptions:

1. The helix on constrained to be on a conical surface of fixed opening angle. A point located on the helix has a distance $R = z \tan \Psi + R_0$ from the helical axis, where Ψ is the half-opening angle and R_0 is the initial distance from the helical axis. The azimuthal coordinate of the point is

$$\phi(z) = \pm 2\pi \int_{z1}^{z} \frac{dz'}{\lambda(z')} + \phi_1 \,, \tag{2}$$

where $\lambda(z)$ is the helix wavelength and ϕ_1 and z_1 are initial values of the azimuth angle and z (distance along helical axis), respectively. The choice of sign for ϕ is determined by the handedness of the helix.

2. The wavelength of the helix is assumed to increase as a power-law function of distance along the conical surface:

$$\lambda(z) = \lambda_1 (R/R_1)^c \,, \tag{3}$$

where $\lambda_1 \equiv \lambda(z_1)$ and $R_1 \equiv R(z_1)$. The parameter c ranges from 1 to 1.5, with $c = 1.5$ describing the adiabatic expansion of a light jet. Note that we could not find solutions for the isothermal case ($c = 1$) which provided a good fit to the trajectory of any component. This is apparently because the observed trajectories become straighter (i.e., increasing helical wavelength) with core distance. This is contrary to the $c = 1$ case, which requires a constant helical wavelength. We therefore used the adiabatic model ($c = 1.5$) for all calculations.

3. Each component has a constant Lorentz factor γ and therefore a constant speed β along the helical path. Hence, observed variations in apparent speed are due to time delays caused by the jet curvature.

4. Shocks are formed near the vertex with random initial conditions, but the helical geometry (e.g., opening angle,

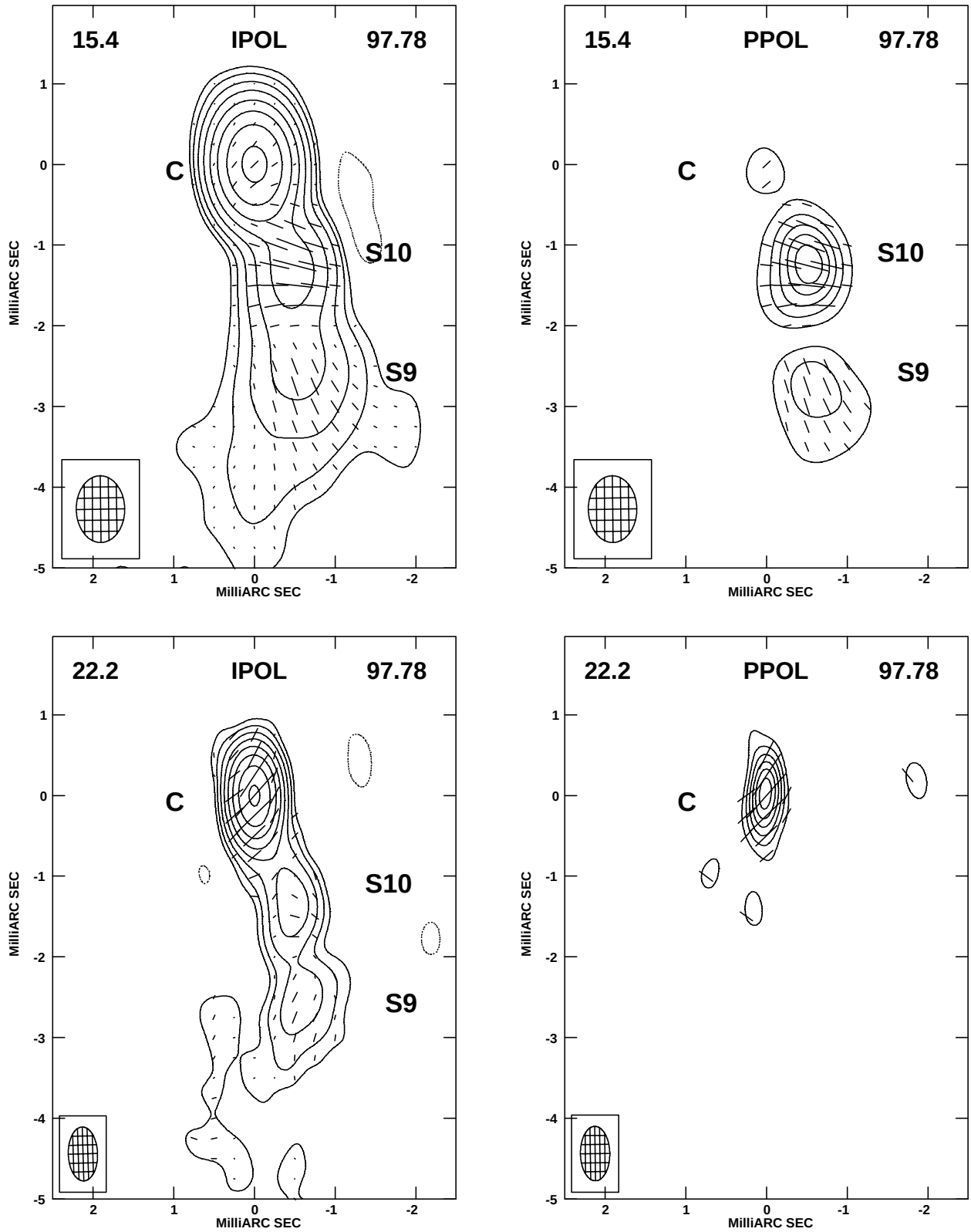

FIG. 13.—Maps of BL Lac in Stokes I and total linear polarization at 15.4 and 22.2 GHz at epoch 1997.78. Contour levels for Stokes I (IPOL) maps are -15, 15, 30, 60, 120, 240, 480, and 960 mJy beam^{-1}. Contours for polarized intensity $(Q^2 + U^2)^{1/2}$ maps (PPOL) are 7.5 (15.4 GHz only), 15, 22.5, 30, 37.5, 45, and 52.5 mJy beam^{-1}.

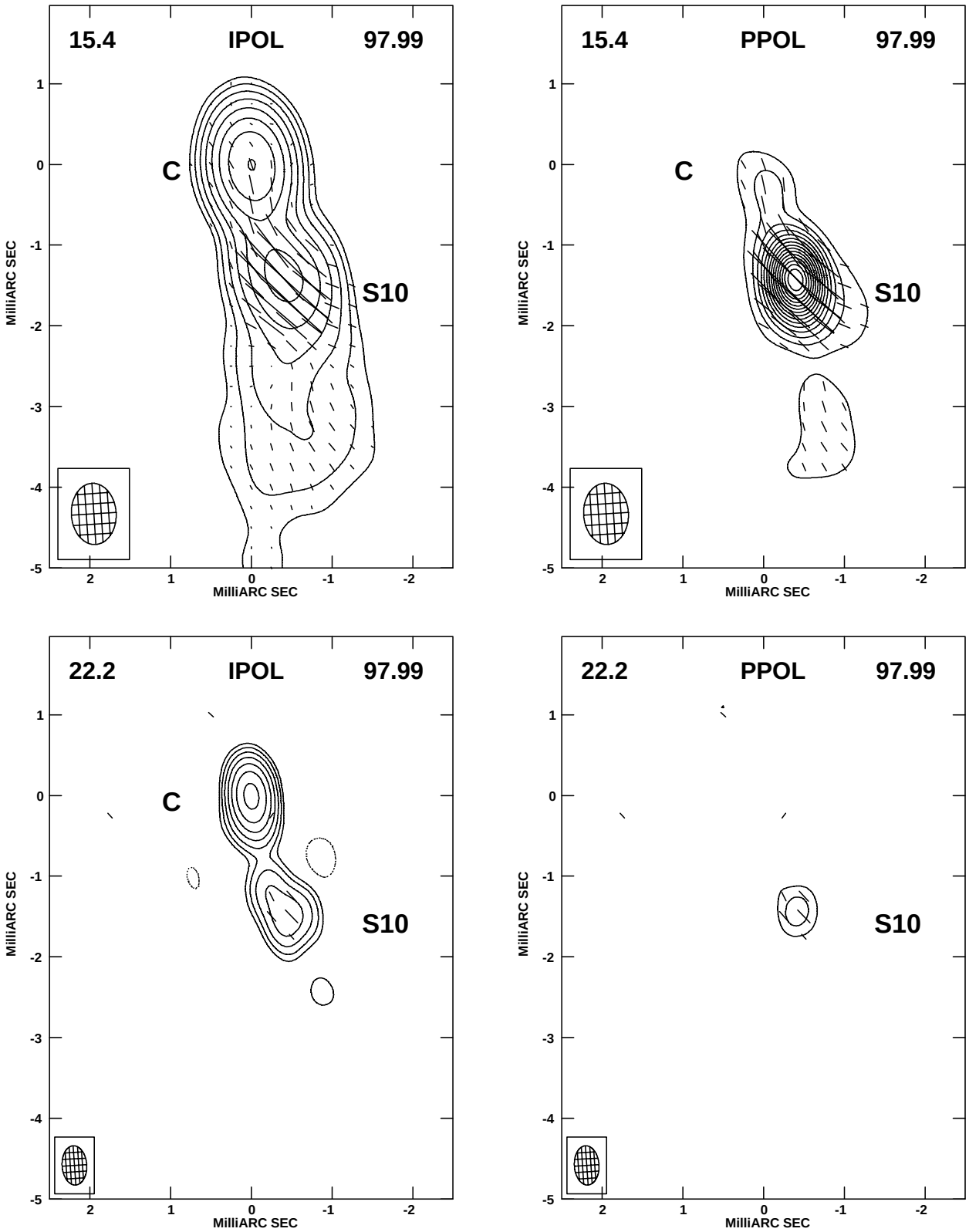

FIG. 14.—Maps of BL Lac in Stokes I and total linear polarization at 15.4 and22.2 GHz at epoch 1997.99. Contour levels for Stokes I (IPOL) maps are -15, 15, 30, 60, 120, 240, 480, and 960 mJy beam^{-1}. Contours for polarized intensity $(Q^2 + U^2)^{1/2}$ maps (PPOL) are 3.75 (22.2 GHz only), 7.5, 15, 22.5, 30, 37.5, 45, 52.5, 60, 67.5, 75, 82.5, 90, 97.5, 105, and 112.5 mJy beam^{-1}.

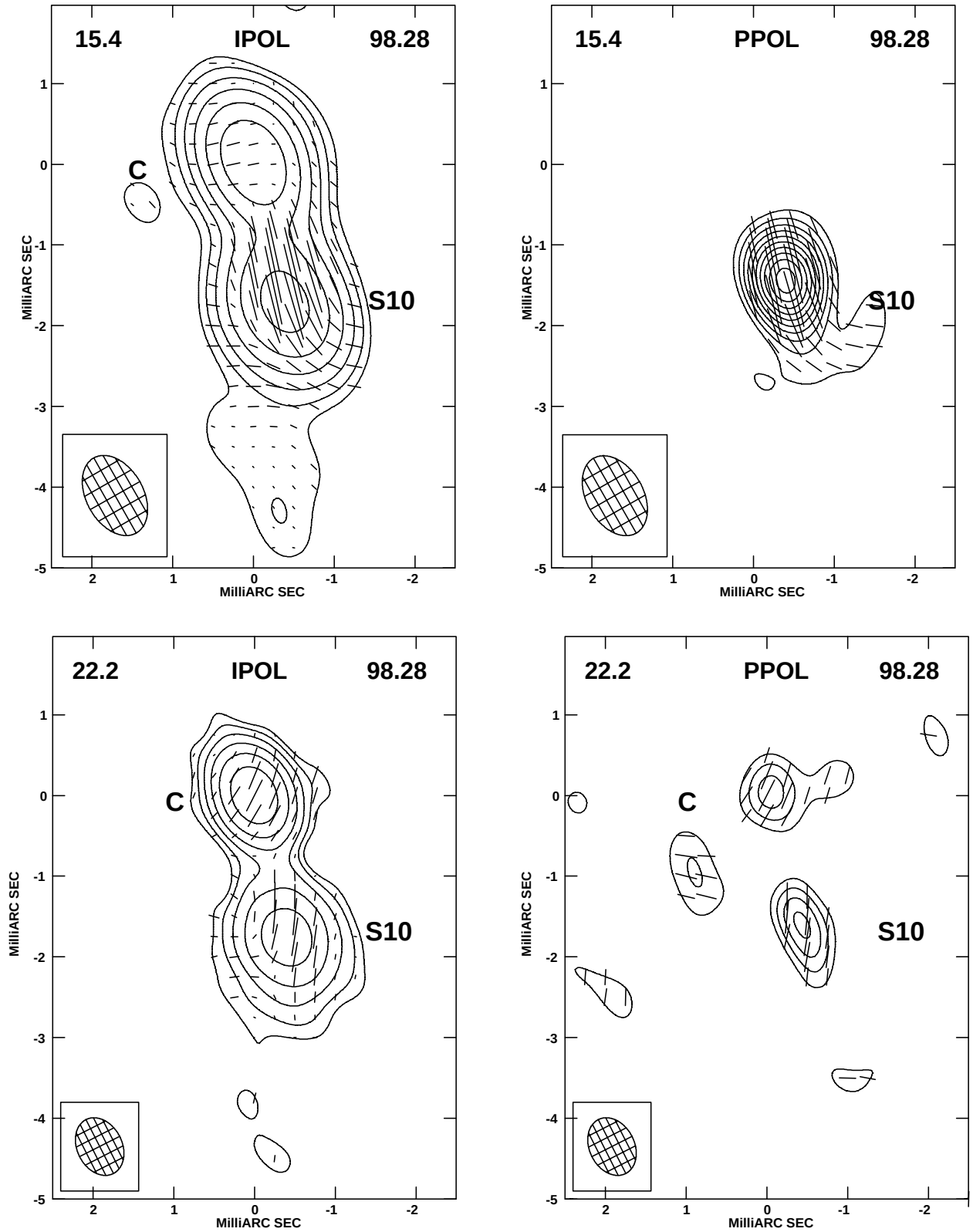

FIG. 15.—Maps of BL Lac in Stokes I and total linear polarization at 15.4, 22.2, and 43.2 GHz at epoch 1998.28. Contour levels for 15.4 and 22.2 GHz Stokes I (IPOL) maps are -30, 30, 60, 120, 240, 480, and 960 mJy beam^{-1}. Contours for 15.4 and 22.2 GHz polarized intensity maps (PPOL) are 75, 150, 225, 300, 375, 450, 525, 600, 675, 750, 825, 900, and 975 mJy beam^{-1}. Contour levels for 43.2 GHz maps are (IPOL) -15, 15, 30, 60, 120, 240, and 480 mJy beam^{-1} and (PPOL) 7.5, 15, and 22.5 mJy beam^{-1}.

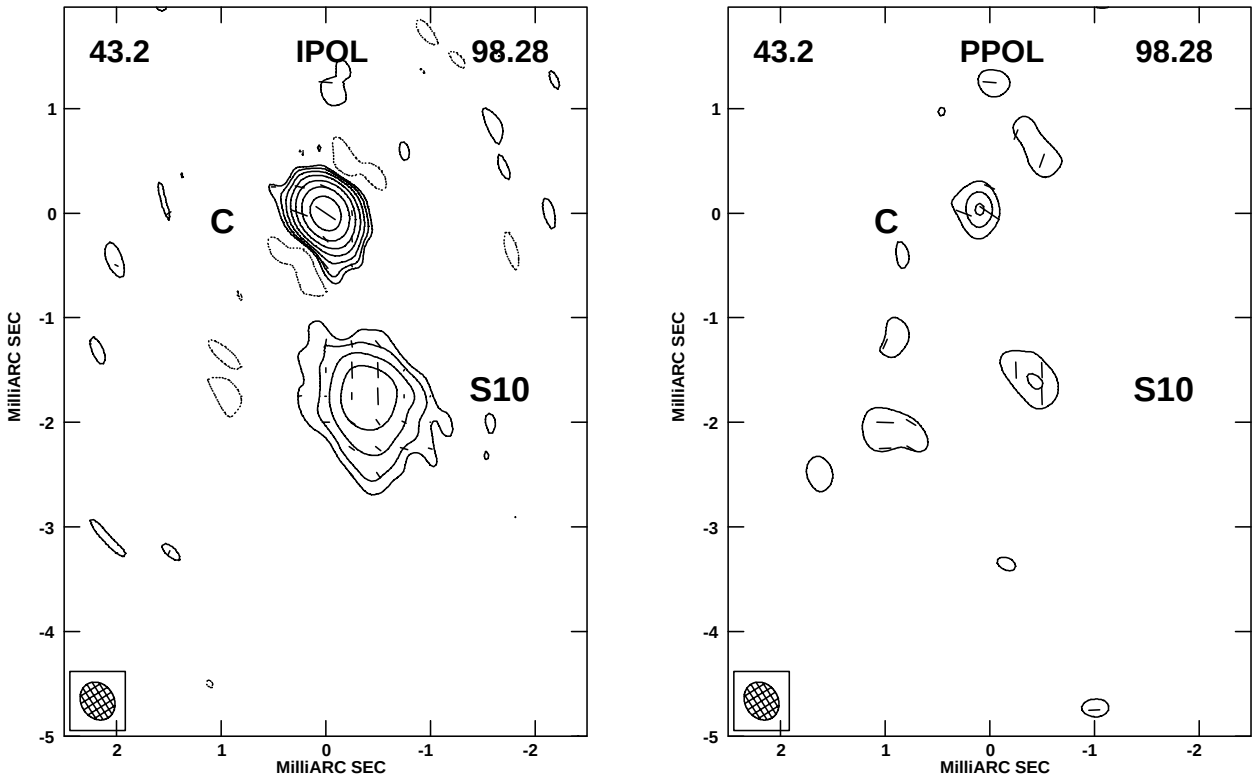

FIG. 15.—*Continued*

orientation to the line of sight) remains fixed over the lifetime of many shock components.

The apparent velocity of a component is given by

$$\beta_a(\theta') = \frac{\beta \sin \theta'}{1 - \beta \cos \theta'}, \quad (4)$$

where θ' is the instantaneous angle of the velocity to the line of sight and can be calculated from

$$\cos \theta' = \cos \Theta \cos \epsilon \cos \Psi - \sin \Theta(\pm \cos \phi \sin \epsilon + \sin \phi \cos \epsilon \sin \Psi), \quad (5)$$

where the sign is determined by the helicity, and where ϵ is the azimuthal rate of deviation, such that $\tan \epsilon = R\, d\phi/dz$. (This expression is equivalent to the equation in Hardee (1987), top of p. 86). The Doppler factor $\delta = \gamma^{-1}(1 - \beta \cos \theta')^{-1}$ and the flux increase $S/S_0 = \delta^{2-\alpha}$ (assuming $\alpha = -0.7$) are also calculated. Figure 26 shows θ', β_a, δ, and S/S_0 as a function of core distance.

4.1.1. *Comparison with Trajectories*

We searched parameter space for models in which fits to all four component trajectories have similar values of helical half-opening angle, angle to line of sight, and position angle of the helical axis projected onto the sky. The initial azimuthal angles, radii, and wavelengths are independent for each component. A program was written to evaluate the reduced χ^2 fit over a large range in all parameters. For each component, a fit to the positional data was found for each set of free parameters and the solutions sorted by best fit. Table 3 shows the selected model values of Ψ, Θ (the angle of the helical axis to the line of sight), the initial values of λ, ϕ, R, and z, the position angle of the helical axis on the sky (ξ), and the Lorentz factor γ. The parameter uncertainties are 90% confidence intervals calculated by varying each parameter while holding all others fixed.

In Figure 25, the model trajectory for component S9 is superposed onto a map of the large-scale radio structure of BL Lac. There is a reasonably good agreement between the trajectory and the faint SE radio lobe. This is the case for model trajectories of all four components, although it is not clear that the observed parsec-scale shocks propagate to decaparsec scales.

Although we did not include the core position as part of the trajectory fits for each component, three of the four trajectories intersect the core within 0.1 mas. The only exception is the trajectory for component S7, which has no measured positions closer than 1 mas from the core, and hence is poorly constrained close to the core.

4.1.2. *Comparison with Kinematic Properties*

The beaming angle for all four components reaches a minimum of 4° within the inner 2 mas and then increases to approximately 12°. Component S8 has the most pronounced change in beaming angle, from 17° to 4° over a core distance of 0.5 mas to 1.4 mas. The large variations within the inner 0.3 mas are the result of a small initial wavelength λ_1. The line of sight angle saturates at high core distances to a value $\sim 11°$ for all four models.

Figure 24*b* shows the core-component radial separation as a function of observing epoch along with the expected separation determined form the helical model. The expected separation is nearly linear with epoch at large core distances but is more complicated within ~ 0.5 mas of the core. Unfortunately, it is very difficult to measure the core-component separation at such small angular scales because the component is blended with the core, particularly at lower observing frequencies. For component S10, we were

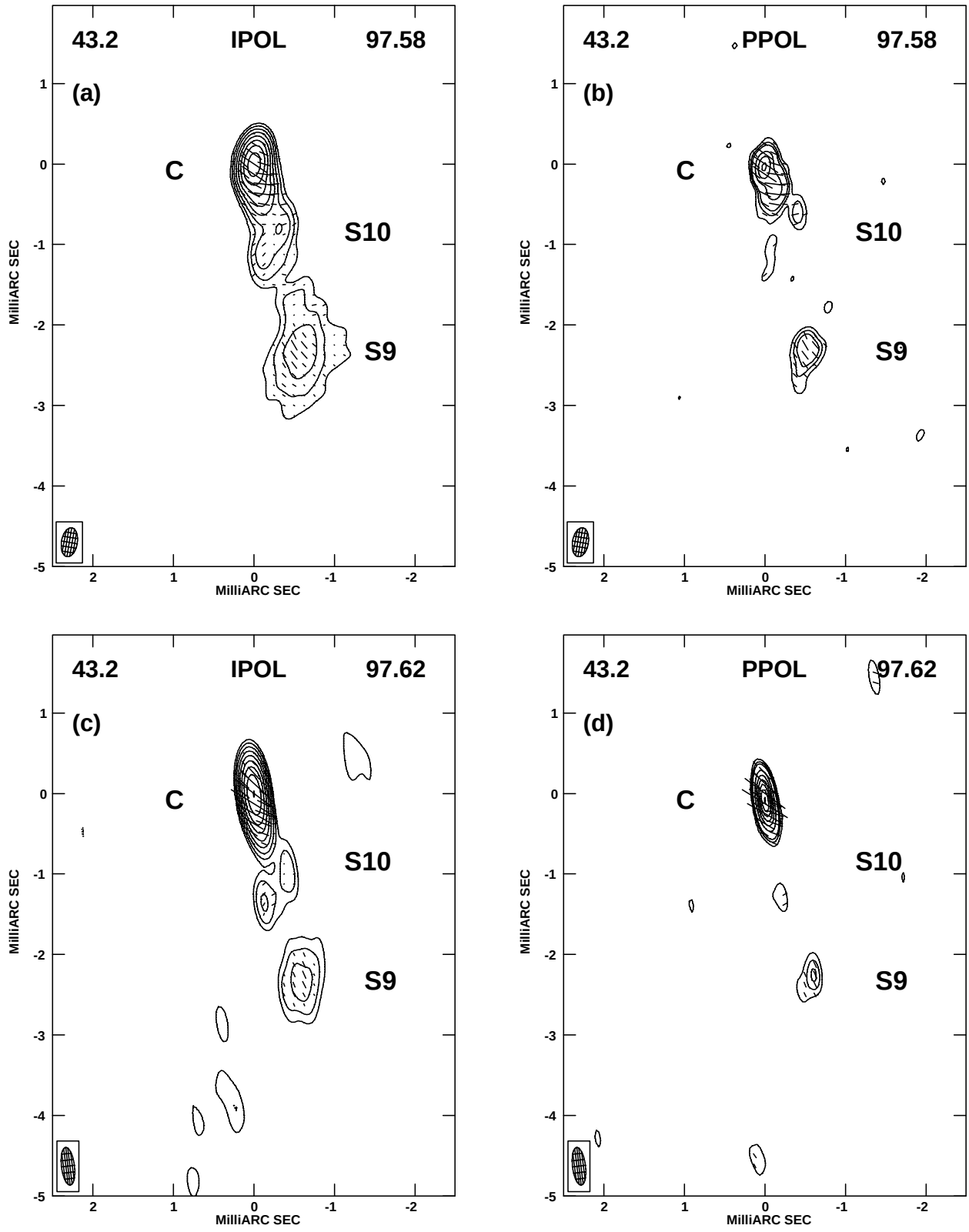

FIG. 16.—43 GHz VLBA maps of BL Lac at two closely spaced epochs: (*a*) Total intensity and (*b*) polarized intensity at epoch 1997.58; (*c*) total intensity and (*d*) polarized intensity at epoch 1997.62. Contour levels for the IPOL maps are -7.5, 7.5, 15, 30, 60, 120, 240, 480 mJy beam^{-1}. Contour levels for the PPOL maps are 3.75, 5.63, 7.5, 15, 22.5, 30, 37.5, and 45 mJy beam^{-1}.

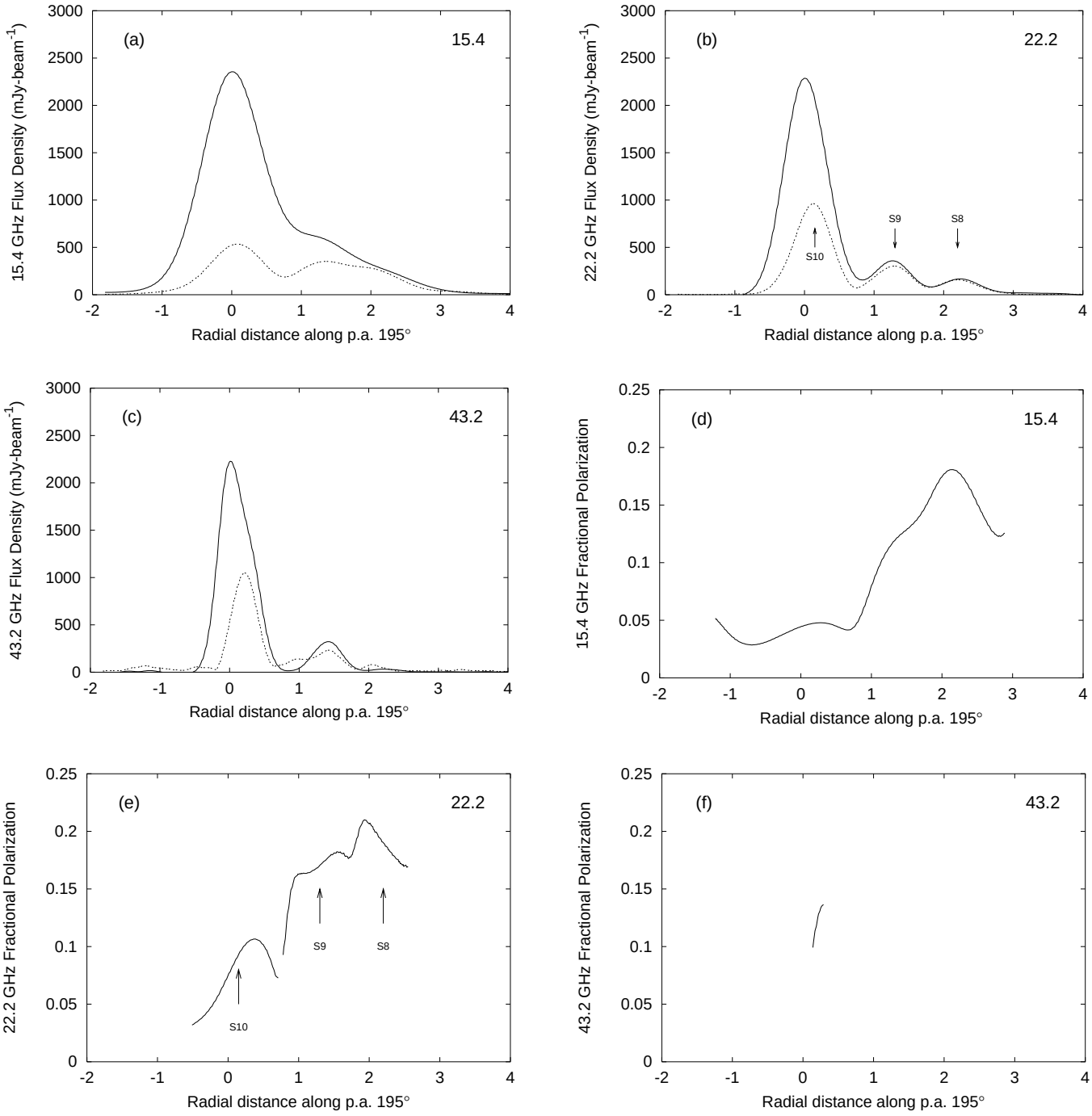

FIG. 17.—(*a–c*) One-dimensional intensity plots of total intensity (*solid lines*) and polarized intensity (*dashed line*) along p.a. 195° at 15.4, 22.2 and 43.2 GHz at epoch 1996.95. The polarized intensity plots have been multiplied by a factor of 5.0 for clarity. (*d–f*) Fractional polarized intensity vs. radial distance along p.a. 195°.

able to utilize 43 GHz maps to measure component position within 0.5 mas, but the fit does not reproduce the observations very successfully.

Apparent speeds were determined from equation (4). The values of β were chosen to fit the observed apparent speeds at large distances from the core. Doppler factors for components S7, S8, and S9 reach maxima near 1.0 and 1.8, and 0.5 mas, respectively (Fig. 26), close to the observed flux maxima (cf. Table 2). However, component S10 is predicted to be brightest within 0.5 mas, but the observations show a rebrightening past 1.5 mas, but consistent with the model.

4.1.3. *Comparison with Observed EVPA*

A shock front traveling parallel to the jet flow will compress the jet magnetic field in a plane perpendicular to the instantaneous direction of the shock motion. If the underlying jet has a random magnetic field orientation, the observed EVPA of a synchrotron emitting region located in

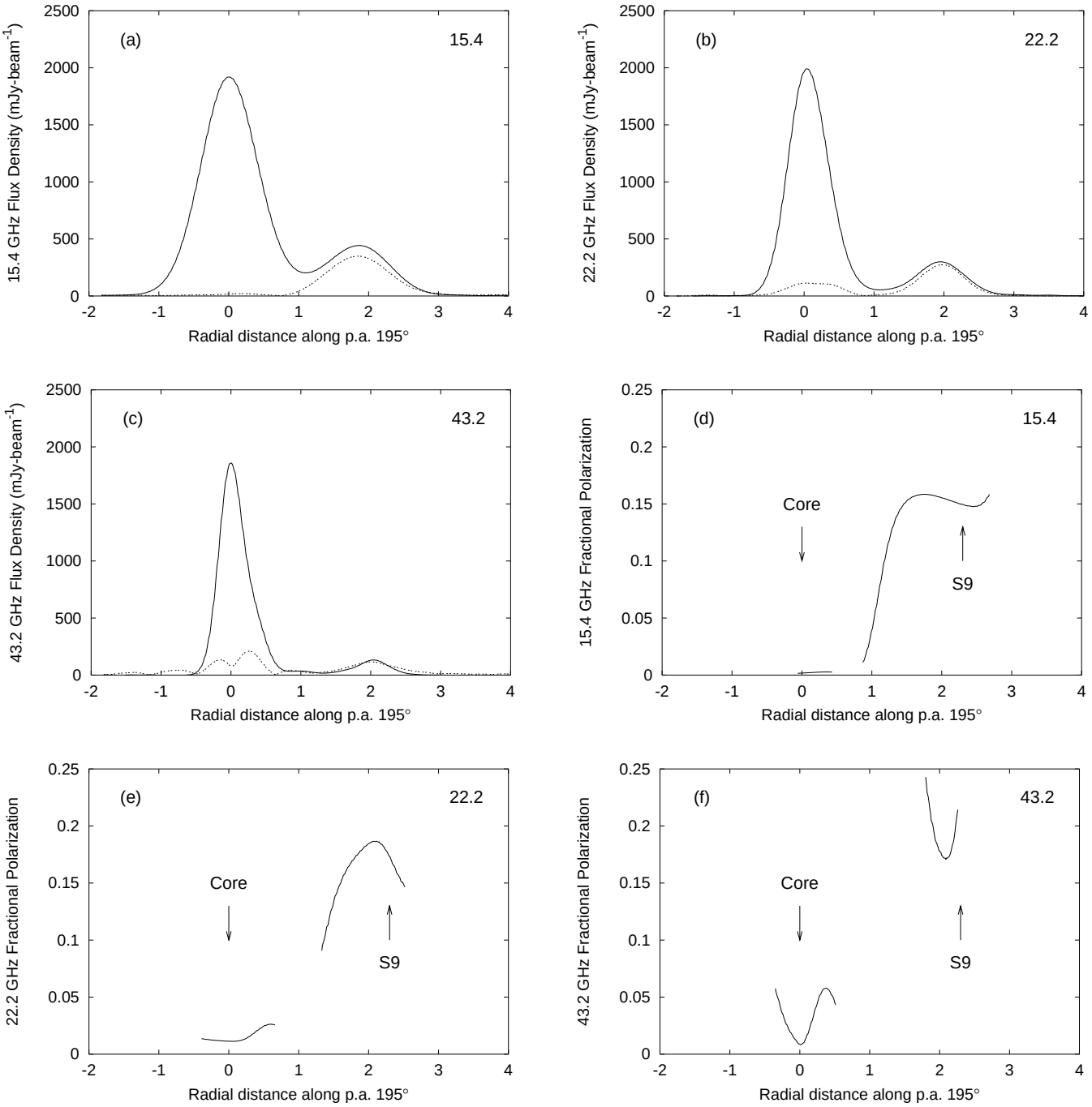

FIG. 18.—(*a–c*) One-dimensional intensity plots of total intensity (*solid lines*) and polarized intensity (*dashed line*) along p.a. 195° at (*a*) 15.4, (*b*) 22.2, and (*c*) 43.2 GHz at epoch 1997.36. Polarized intensities have been multiplied by a factor of 5.0 for clarity. (*d–f*) Fractional polarized intensity vs. radial distance along p.a. 195°.

the post shock plasma will be oriented perpendicular to the compressed magnetic field, and hence parallel the shock velocity vector projected onto the sky plane. The observed EVPA may be quite different from the intrinsic EVPA if the transverse dimension of the shock is large enough to cause aberration due to relativistic time delays (Blandford & Königl 1979) or optical depth effect (Gomez et al. 1995). As previously discussed (Fig. 27), the initial EVPAs of all four components are randomly oriented with respect to direction of the shock, although there is a tendency for the EVPA to become parallel to the direction of motion as the shock moves away from the core. This may indicate that relativistic aberration effects are more important when the shock is young, or that shocks are formed at arbitrary oblique angles but gradually evolve into transverse shocks as they propagate down the jet. We have not included these effects in this analysis.

4.2. *Application of Relativistic Shock Model*

We now obtain constraints on the physical properties of superluminal components using the relativistic shock model (e.g., Hughes et al. 1985; Kollgaard, Wardle, & Roberts

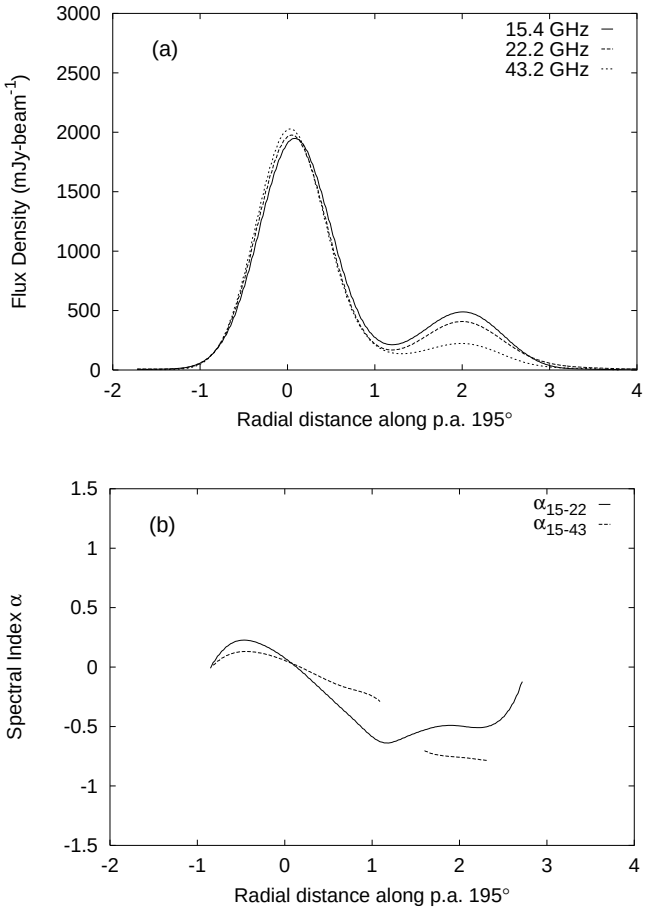

FIG. 19.—(*a*) One-dimensional plots of total intensity along p.a. 195° at 15.4 GHz (*solid line*), 22.2 GHz (*dashed line*) and 43.2 GHz (*dotted line*) at epoch 1997.36. The 22.2 and 43.2 GHz maps were convolved with the 15.4 GHz restoring beam before one-dimensional plots were computed. (*b*) Two-point spectral index ($S \propto \nu^{\alpha}$) along p.a. 195° using (15.4, 22.2) GHz and (15.4, 43.2) GHz frequency pairs.

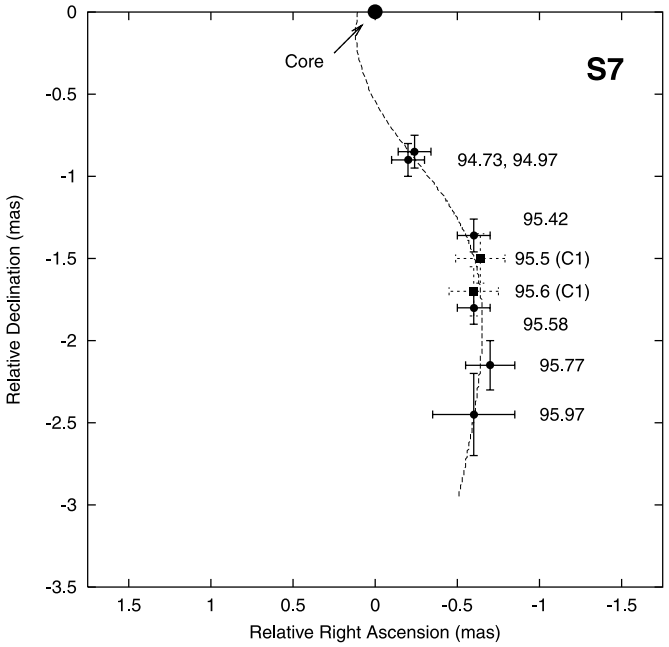

FIG. 20.—Positions of component S7 with observing epochs labeled. The positions of component C1 from Tateyama et al. (1998), which we have identified with component S7 are also shown. The dashed line is the model fit to the component's trajectory using the helical model parameters shown in Table 3.

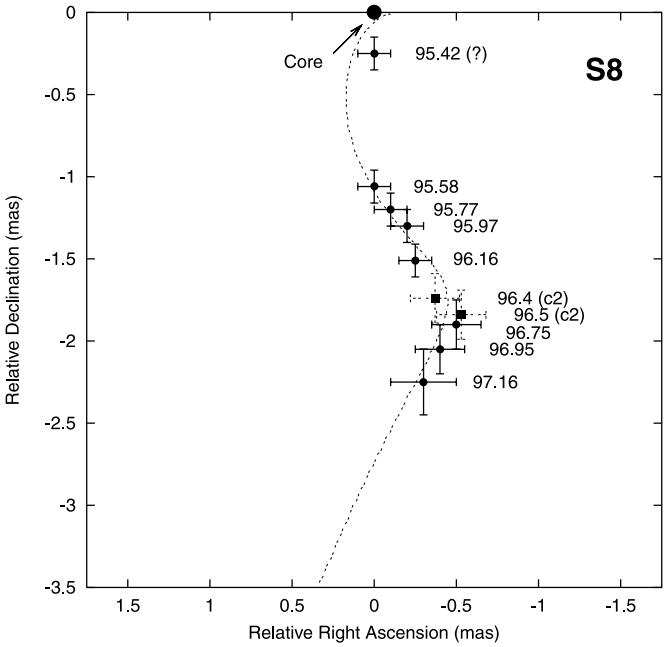

FIG. 21.—Positions of component S8 with observing epochs labeled. The positions of component C2 from Tateyama et al. (1998), which we have identified with component S8 are also shown. The dashed line is the model fit to the component's trajectory using the helical model parameters shown in Table 3.

1990; Wardle et al. 1994). The model is used to constrain the shock compression ratio (and therefore the Lorentz factor of the jet) and the angle of the jet direction to the line of sight. Note that this analysis assumes transverse shocks, which not may be strictly applicable to the components in BL Lac as discussed above.

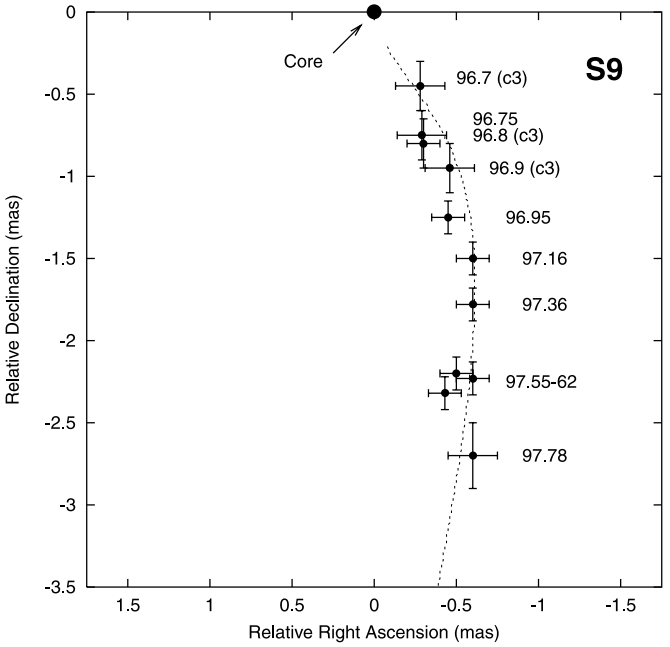

FIG. 22.—Positions of component S9 with observing epochs labeled. The positions of component C3 from Tateyama et al. (1998), which we have identified with component S9 are also shown. The dashed line is the model fit to the component's trajectory using the helical model parameters shown in Table 3.

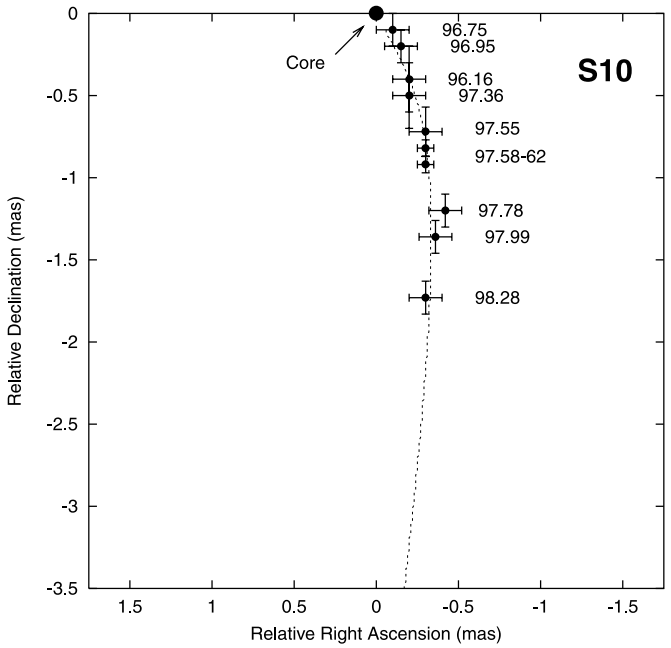

FIG. 23.—Positions of component S10 with observing epochs labeled. The dashed line is the model fit to the component's trajectory using the helical model parameters shown in Table 3.

The observed fractional polarization, ratio of the knot to interknot brightness, and apparent speed constrain the angle between the instantaneous jet direction and the line of sight. The preshocked (upstream) magnetic field is assumed to be initially tangled with no preferred direction. It is compressed by a shock passage in a plane parallel to the jet flow. The compressed region accelerates electrons that radiate via synchrotron emission. The compression k in the shock is the ratio of downstream to upstream densities, given by

$$k = \frac{n_u}{n_d} = \frac{\gamma_d \beta_d}{\gamma_u \beta_u}, \tag{6}$$

where the subscripts refer to upstream (u) and downstream (d) velocities in the shock's comoving frame.

The expected fractional polarization in a shocked region emitting optically thin synchrotron radiation is (Wardle et al. 1994)

$$m_d = m_0 \left[\frac{(1 - k^2) \sin^2 \theta_d}{2 - (1 - k^2) \sin^2 \theta_d} \right], \tag{7}$$

where $m_0 = (3 - 3\alpha)/(5 - 3\alpha)$ is the maximum fractional polarization, and θ_d is the angle between the flow direction of the downstream material and the line of sight in the observer's frame. The ratio of downstream to upstream intensity is a function of the upstream and downstream Doppler factors δ_u and δ_d (calculable from the jump conditions and the observed superluminal velocity):

$$\frac{I_d}{I_u} = \left[1 - \frac{1}{2} (1 - k^2) \sin^2 \theta_d \right] k^{(2\alpha - 9)/3} (\delta_d/\delta_u)^{2-\alpha}. \tag{8}$$

Contours of I_d/I_u and m_d were plotted in the (k, θ') plane. We used viewing angles determined from the helical model (Table 3) to constrain the allowed viewing angles for the shock model: $\theta' \simeq 5°$–$10°$. We were unable to find a consistent set of solutions in this range unless we chose a Hubble parameter h significantly less than one. By adopting $h = 0.5$, we found a set of viewing angles for all four components that were consistent with both the shock model for the components and helical model for the jet.

The components had variable polarization over their lifetimes; we used the mean fractional polarization for the model. For components S7–S10, this was $m_d = 0.11$, 0.12, 0.23, and 0.10, respectively. The downstream values I_d are the shock values, but the absence of the "naked jet" leaves the value of I_u undetermined.

In Figure 28 we show a representative plot of m_d and I_d/I_u in the (θ', k) plane for component S8 using a nominal spectral index $\alpha = -0.7$ (cf. § 3.2.2.1). The intensity ratio contours range from $I_d/I_u = 1$ to 32, and the m_d contours are values from Table 2, assuming $m_d \approx m_L$. Table 4 contains a summary of the model parameters. Column (4) (k) lists the allowed shock compression without the constraints on β_u and θ', and column (6) ($k_{\rm con}$) shows the range of allowed compression ratios using the line of sight angle determined from the helical model (Table 3). When the viewing angle constraints derived from the helical model are

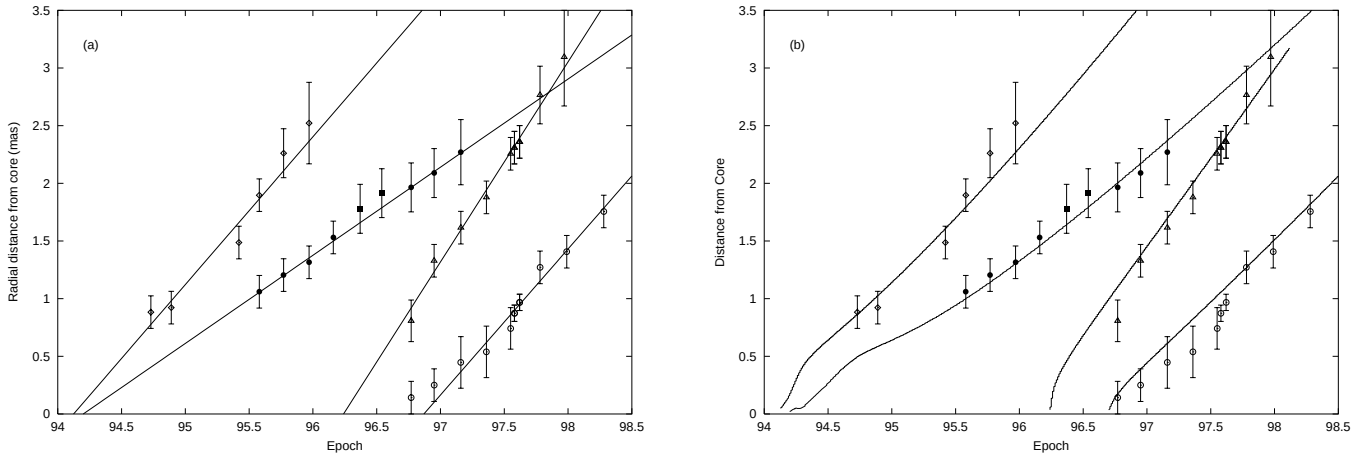

FIG. 24.—Core-component radial separation as a function of epoch for components S7 (◇), S8 (●), S9 (△), and S10 (○). Solid lines indicate: (*a*) Least-square linear slope for each component. The best-fit speeds are $\beta = (3.7 \pm 0.4)\,h^{-1}$, $(2.2 \pm 0.1)\,h^{-1}$, $(5.4 \pm 0.4)\,h^{-1}$, and $(2.8 \pm 0.2)\,h^{-1}$ for components S7–S10, respectively. Corresponding creation dates are $t_0 = 1994.12 \pm 0.13$, 1994.20 ± 05, 1996.31 ± 0.08, 1996.87 ± 0.06. (*b*) Radial distance vs. epoch predicted using helical model parameters. Note that each component of the pairs (S7, S8) and (S9, S10) appear to have been ejected from the core close to the same epoch.

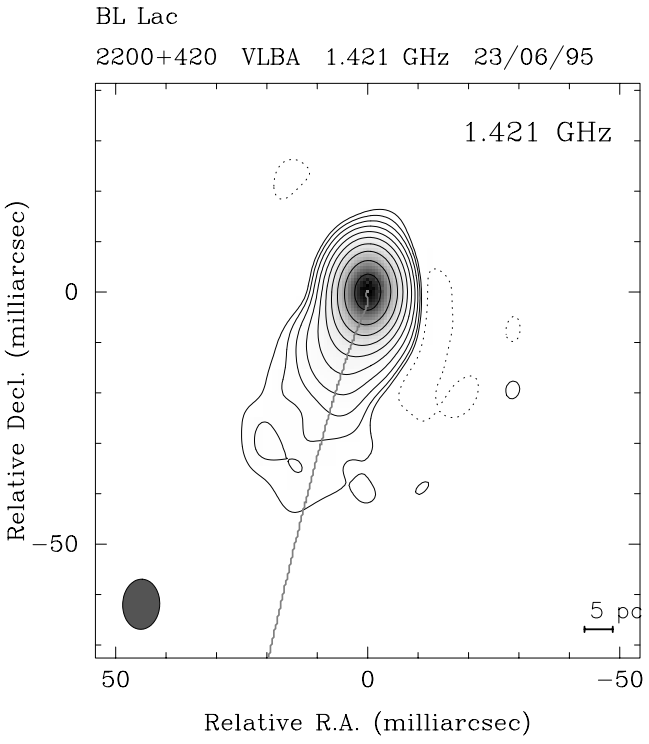

FIG. 25.—VLBA Map of BL Lac at 1.42 GHz showing extended faint jet south of the core. The overlaid gray line shows the trajectory of component S9 using the helical model parameters in Table 3. Contour levels are −4, 4, 8, 16, 32, 64, 128, 256, 512, 1024, 2048, and 4096 mJy beam^{-1}.

imposed, forward shocks solutions are favored for S8 (Fig. 28*a*, *shaded region*) and S10, while both S7 and S9 have solutions allowing either forward or reverse shocks. Shock compressions are weak ($k < 0.5$) for all components with the exception of component S9, which has solutions favoring high compression ($0 < k < 0.5$).

We can compare these results to recent analyses of VLBP images of two other AGNs. Wardle et al. (1994) found that component C3 in the quasar 3C 345 at was consistent with a weak forward moving shock. Leppänen (1995) observed component C7 in 3C 345. He also finds the observations consistent with a forward shock, but with a compression ratio significantly higher than in C3 ($k = 0.3$ vs. 0.7). Though the compression may be a function of core distance, the electric field vectors during this epoch were aligned with the jet. Therefore, the nature of C7 may be quite different from that of C3. An analysis of component K2 in the BL Lac object OJ 287 by Cawthorne & Wardle (1988) found that a reverse shock was favored. It was suggested in Wardle et al. (1994) that perhaps all BL Lac objects have reverse shocks, whereas all quasars have forward moving shocks. Our results do not support this conjecture.

4.3. *The Optical–Gamma-Ray Flare of 1997 July*

In mid-July of 1997, BL Lac underwent an period of intense flaring activity at optical and gamma-ray wavelengths. There was a prolonged period of optical flaring (Noble et al. 1997; Nesci et al. 1998), including several rapid fluctuations of up to 1.5 mag in a single day (Maesano et al.

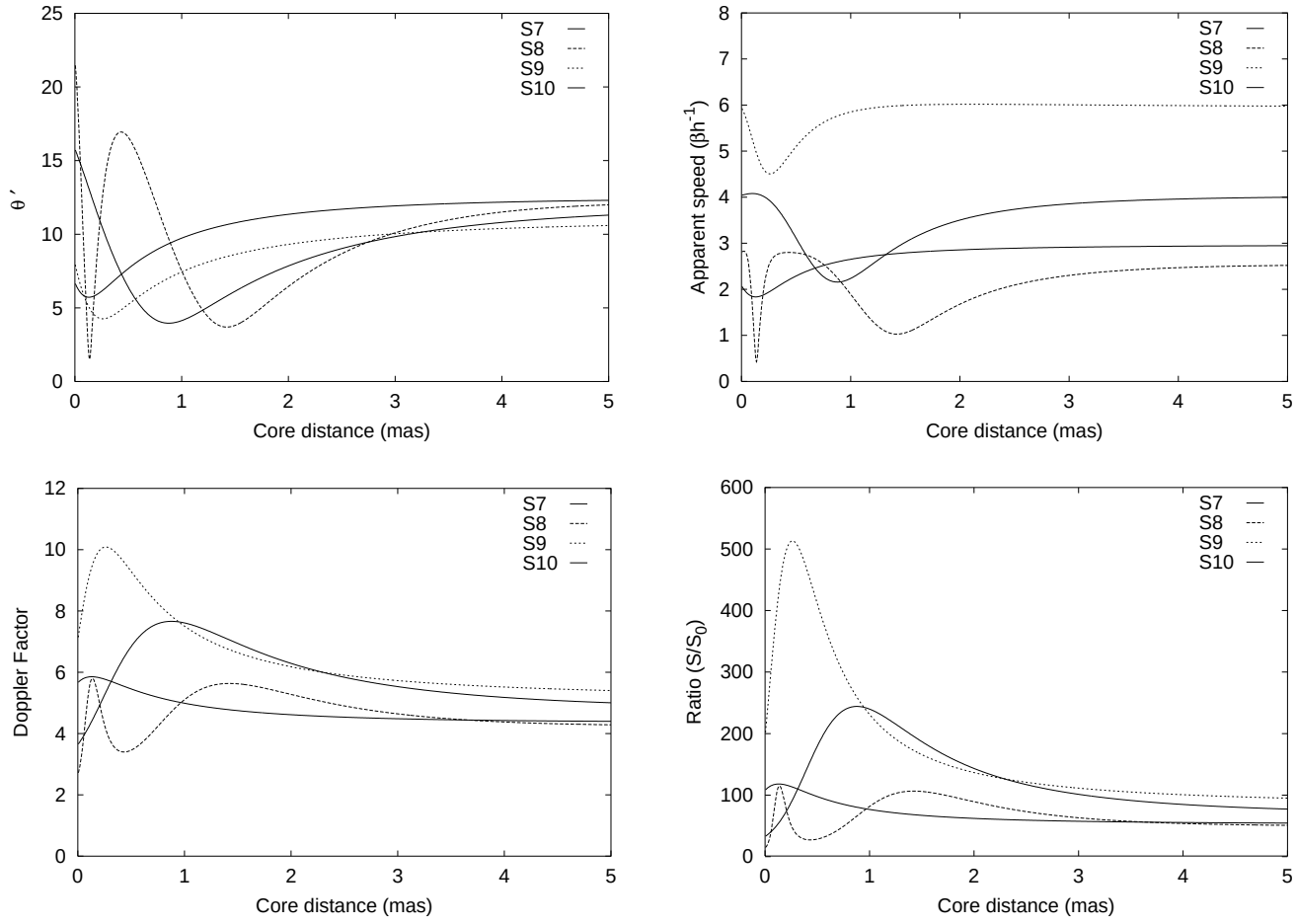

FIG. 26.—Helical model parameters as a function of core distance. (*a*) Beaming angle; (*b*) Apparent velocity; (*c*) Doppler factor; (*d*) Doppler boosted flux ratio.

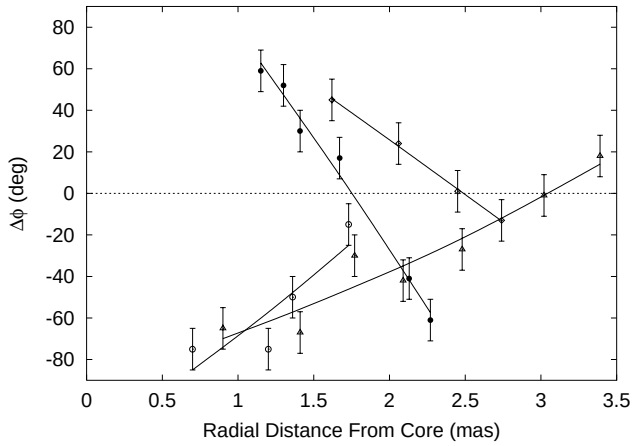

FIG. 27.—Difference between EVPA and trajectory tangent direction vs. core-component radial distance for components S7 (◇), S8 (●), S9 (△), and S10 (○). The lines are smooth spline fits. The expected difference is zero degrees (*dashed line*) for synchrotron emission from an ideal plane-perpendicular shock.

1997). The flare was also detected as a gamma-ray flare at energies above 100 MeV by the EGRET instrument on board the *Compton Gamma Ray Observatory* (Bloom et al. 1997) at more than four times the highest flux previously recorded for this source. Such energetic events are thought to be associated with the generation of shocks or other strong instabilities in the inner accretion disk of the AGN, e.g., (Wagner & Witzel 1995). Gamma-ray emission in AGNs is thought to be generated by either synchrotron-self-Compton or inverse-Compton processes in the innermost part of the jet close to the central energy source. In either case, acceleration of highly relativistic electrons is expected, with consequent synchrotron radiation in the radio regime. In support of this scenario, Zhou et al. (1997) have reported a correlation between the EGRET gamma-ray flux and the VLBI-determined core radio flux for a sample of 31 AGN sources.

The parsec-scale structures seen in VLBI maps can only be affected after the disturbance has had time to propagate at least to the base (core) of the radio jet. Otterbein et al. (1998) began VLBI monitoring of the quasar 0836+710 shortly after a similar optical–gamma-ray outburst in early 1992. They found that a superluminal component (B3, $\beta = 10\ h^{-1}$) was ejected from the radio core at epoch 1992.6, about six months after the offset of optical-gamma-ray activity. The authors calculate the expected time delay between the onset of activity at the vertex of a conical jet ("jet nozzle," where the optical–gamma-ray flare presumably originates) and the VLBI core using a model for the jet which assumes that the component is in the adiabatic loss phase (Marscher & Gear 1985). The nozzle-core time delay for a jet disturbance with constant Doppler factor along the jet is given by

$$\Delta t = \frac{r_1(1+z)}{\gamma\delta\beta c}\,, \tag{9}$$

where z is the redshift, r_1 is the vertex-core distance, γ is the Lorentz factor, δ is the Doppler factor, and β is the speed of the disturbance. The vertex-core distance was estimated to be $r_1 \approx 10$ pc for 0836+710 (Lobanov 1998), resulting in a time delay of $\Delta t = 0.74 \pm 0.07$ yr, in good agreement with the appearance of B3 vis-a-vis the optical burst.

Since the optical–gamma-ray outburst of BL Lac at epoch ~1997.6, we have continued to monitor the parsec-scale radio structure but have not (yet) detected a new superluminal component up to epoch 1998.28. In addition, there has not been a flux outburst at centimeter wavelengths (Fig. 1). Either the optical/gamma-ray burst has not affected the parsec-scale jet, or the vertex-core time delay exceeds $\Delta t = 0.9$ yr. In the latter case, we can estimate the minimum vertex-core separation using the observed values of apparent speed and line-of-sight angles derived for components S7–S10 from the helical model (Table 3). We calculate minimum vertex-core distances range from 4 pc (S7) to 11 pc (S9) using values for the slowest (S7) and fastest (S9) components. Since new shock components arise about every year or two in BL Lac, it will be difficult to causally connect the appearance of a new component with the 1997 June outburst unless the nature of the component differs appreciably from previous components.

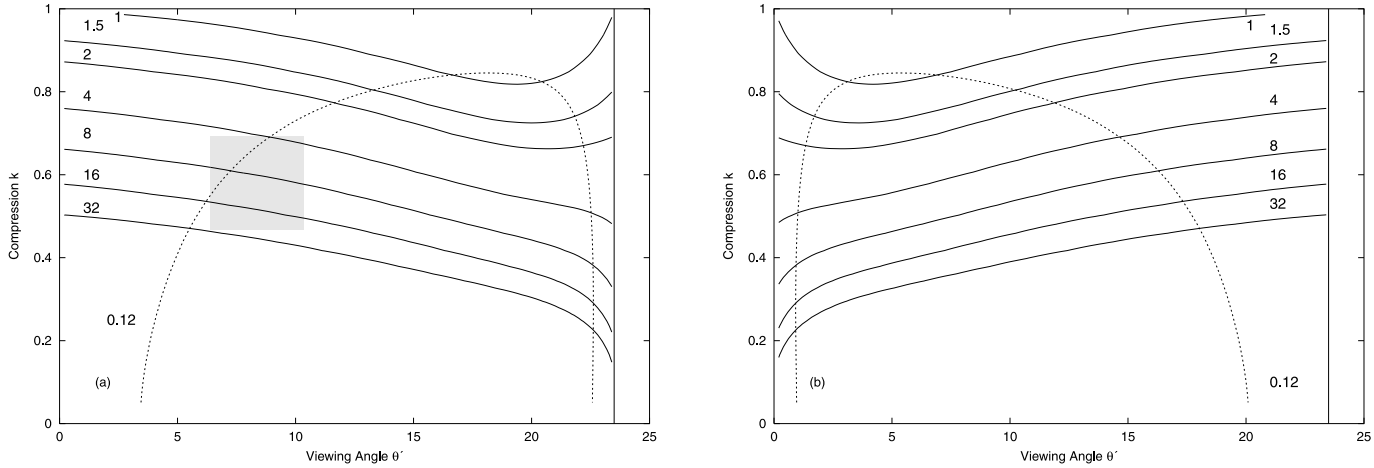

FIG. 28.—Contours of fractional polarization and knot to interknot intensity ratio for component S8 as a function of viewing angle and shock compression. Solutions to the right of the solid vertical line are forbidden by the observed apparent velocity. Solid lines are downstream to upstream intensity ratios $I_d/I_u = 1$, 1.5, 2, 4, 8, 16, and 32; the dotted line indicates the observed mean fractional component polarization $m_d = 0.12$. Note that the helical model predicts a viewing angle $\theta \sim 9°$. Since the observed knot-interknot intensity ratio is $\gtrsim 10$, a forward shock with compression ratio $k \sim 0.6$ is favored (*shaded region*).

5. CONCLUSIONS

We have monitored the radio core of BL Lacertae at centimeter and millimeter wavelengths for 17 epochs spanning epochs 1994.73–1998.28.

The major observational results of this study are the following:

1. We observed four superluminal components (denoted S7, S8, S9, and S10) emerge from an assumed stationary core over a 4 year period between epochs 1994.71 and 1998.28. All four components were detected at multiple epochs with nearly constant apparent speeds of $\beta = (3.7 \pm 0.4)\ h^{-1}$ (S7), $\beta = (2.2 \pm 0.1)\ h^{-1}$ (S8), $\beta = (5.0 \pm 0.2)\, h^{-1}$ (S9), and $\beta = (3.7 \pm 0.3)\, h^{-1}$ (S10).

2. Assuming a constant speed from the time of core separation, component "birth"" epochs appear to be paired: $t_0 = (1994.12 \pm 0.13,\ 1994.20 \pm 0.05)$ for (S7, S8), and $(1996.24 \pm 0.05,\ 1996.87 \pm 0.06)$ for (S9, S10). This is clearly illustrated in Figure 24.

3. Component trajectories (Figs. 20–23) are bent, with the degree of bending being largest for the slowest moving component (S8) and smallest for the fastest (S9). Each component propagates with a somewhat independent trajectory, suggesting that the helical structure of the jet in BL Lac is unstable for timescales greater than a few shock traversal times ($\sim$1–2 yr) and does not maintain a constant large-scale geometry for several jet epochs.

4. The observed fractional linear polarization of all four components is time variable both in magnitude and electric field position angle (EVPA; Fig. 27) as the components evolve away from the core. There is no preference for the initial position angle to be aligned either parallel or perpendicular to the jet axis in the inner 2 mas, but there is a trend towards parallel alignment (perpendicular magnetic field) beyond this point. However, component S7 has a nearly perpendicular EVPA at all observed epochs. Component S8 had the largest swing in polarization angle (from $-30°$to $+40°$) The average fractional polarization is $\sim$10%–15%.

5. The fractional polarization of the core is usually low (less than %1). High core polarizations observed immediately prior to component ejections are most likely due to core-component blending. The percentage of core polarization is variable and increases with frequency for epochs where we have good maps.

6. We detected no obvious change in the parsec-scale radio structure of BL Lac which could be attributed to the optical–gamma-ray outburst at epoch 1997.6. During three epochs since the outburst (through 1998.28, Figs. 17–19) there have been no new shock components, although there were two minor flux events at epochs 1997.9 and 1998.3 (Fig. 1).

We have used these observational data to deduce a number of physical properties of the radio jet and knots. We have assumed that the radio emission arises from optically thin synchrotron emission in the compressed downstream material from shocks within a relativistic flow.

1. We have modeled the trajectories, apparent velocities and Doppler factors for four superluminal components using the light adiabatic jet model of Hardee (1987). Our results are consistent with a helical flow, with half-opening angle $2\overset{\circ}{.}1 \pm 0\overset{\circ}{.}4$, and helical axis at an angle of $9° \pm 2°$ to the line of sight. The model fits component trajectories and speeds satisfactorily but does not convincingly predict the observed Doppler boosting and EVPA rotation. Extrapolation of all four component trajectories to decaparsec scales are in good agreement with the observed decaparsec radio structure.

2. By combining the geometrical constraints of the helical model with a relativistic shock model for the emission, we find that three of the four components are weak shocks ($k \geq 0.5$), whereas component S9 is consistent with a strong shock ($k \leq 0.4$). Components S7 and S9 can be modeled with both forward and reverse shocks, while components S8 and S10 are only consistent with forward shocks.

This paper has made use of data from the University of Michigan Radio Astronomy Observatory which is supported by the National Science Foundation and by funds from the University of Michigan. We thank Steve Unwin, Joan Wrobel, Kari Leppänen, Greg Taylor, Jim Ulvestad, and Margo Aller for their advice and assistance. We thank John Wardle for numerous suggestions for improvement of the paper.

REFERENCES

Blandford, R. D., & Königl, A. 1979, ApJ, 232, 24
Bloom, S. D., et al. 1997, ApJ, 490, 148
Cawthorne, T. V., & Wardle, J. F. C. 1988, ApJ, 332, 696
Cawthorne, T. V., Wardle, J. F. C., Roberts, D. H., & Gabuzda, D. C. 1993, ApJ, 416, 519
Conway, J. E., & Wrobel, J. M. 1995, ApJ, 439, 98
Cotton, W. D. 1993, AJ, 106, 1241
Cotton, W. D., Geldzahler, B. J., Marcaide, J. M., Shapiro, I. I., & Ruis, A. 1984, ApJ, 286, 503
Gabuzda, D. C., & Cawthorne, T. V. 1996, MNRAS, 283, 759
Gabuzda, D. C., Cawthorne, T. V., Roberts, D. H., & Wardle, J. F. C. 1992, ApJ, 388, 40
Gabuzda, D. C., Wardle, J. F. C., & Roberts, D. H. 1989, ApJ, 338, 743
Gomez, J. L., Alberdi, A., Marcaide, J., Marscher, A., Travis, J. P. 1995, A&A, 292, 33
Hardee, P. E. 1987, ApJ, 318, 78
Hughes, P. A., Aller, H. D., & Aller, M. F. 1985, ApJ, 298, 301
———. 1989, ApJ, 341, 68
Hutchinson, J. M., & Cawthorne, T. V. 1997, Vistas Astron., 41, 231
Kollgaard, R. I., Wardle, J. F. C., & Roberts, D. H. 1990, AJ, 100, 1057
Königl, A. 1981, ApJ, 243, 700
Leppänen, K. 1995, Ph.D. thesis, Helsinki Univ. Technology
Leppänen, K., J., Zensus, J. A., & Diamond, P. J. 1995, AJ, 110, 2479
Lobanov, A. P. 1998, A&A, 330, 79
Maesano, M., Montagni, F., Massaro, E., & Nesci, R. 1997, IAU Circ. 6700
Marscher, A. P., & Gear, W., K. 1985, ApJ, 298, 114
Massi, M., Rioja, M., Gabuzda, D., Leppänen, K, Sanghera, H., Ruf, K., & Moscadelli, L. 1997, A&A, 318, L32
Miller, J. S., French, H. B., & Hawley, S. 1978, in Pittsburgh Conference on BL Lac Objects, ed. A. Wolfe (Pittsburgh: Univ. Pittsburgh), 176
Mutel, R. L., Phillips, R. B., Su, B., & Bucciferro, R. R. 1990, ApJ, 352, 81
Nesci, R., Maesano, M., Massaro, E., Montagni, F., Tosti, G., & Fiorucci, M. 1998, A&A, 332, L1
Noble, J. C., Carini, M. T., Miller, H. R., Balonek, T. J., Whitman, K., & Davis, S. M. 1997, IAU Circ. 6693
Otterbein, K., Krichbaum, T. P., Kraus, A., Lobanov, A. P., Witzel, A., Wagner, S. J., Zensus, J. A. 1998, A&A, 334, 489
Pearson, T. J., & Readhead, A. C. S. 1988, ApJ, 328, 114
Polatidis, A. G., Wilkinson P. N., Xu, W., Readhead, A. C. S., Pearson, T. J., Taylor, G. B., & Vermeulen, R. C. 1995, ApJS, 98, 1
Roberts, D. H., Gabuzda, D., & Wardle, J. F. C. 1987, ApJ, 323, 536
Roberts, D. H., Wardle, J. F. C., & Brow, L. 1994, ApJ, 427, 718
Rudnick, L., Jones, T. W., Edgar, B. K., & Pedelty, J. A. 1984, AJ, 89, 316

Shepherd, M. C. 1997, in ASP Conf. Ser. 125, Astronomical Data Analysis Software and Systems VI, ed. G. Hunt & H. Payne (San Francisco: ASP), 77
Steffen, W., Zensus, J. A., Krichbaum, T. P., Witzel, A., & Qian, S. J. 1995, A&A, 302, 335
Tateyama, C. E., Kingham, K. A., Kaufman, P., Piner, B. G., de Lucena, A. M. P., & Botti, L. C. L. 1998, ApJ, 500, 810
Taylor, G. 1998, ApJ, 506, 607
Wagner, S. J., & Witzel, A. 1995, ARA&A, 33, 163
Wardle, J. F. C., Cawthorne, T. V., Roberts, D. H., & Brown, L. F. 1994, ApJ, 437, 122
Zhou, Y. Y., Lu, T. G., Wang, K. N., & Young, E. C. M. 1997, ApJ, 484, 47